Applied Catalysis A, General 652 (2023) 119035

Contents lists available at ScienceDirect

Applied Catalysis A, General

journal homepage: www.elsevier.com/locate/apcata

$BiVO_4$ charge transfer control by a water-insoluble iron complex for solar water oxidation

Tímea Benkó [a,*], Shaohua Shen [b], Miklós Németh [a], Jinzhan Su [b], Ákos Szamosvölgyi [c], Zoltán Kovács [d], György Sáfrán [d], Sahir M. Al-Zuraiji [a], Endre Zsolt Horváth [d], András Sápi [c], Zoltán Kónya [c], József Sándor Pap [a]

[a] Centre for Energy Research, Surface Chemistry and Catalysis Department, H-1121, Konkoly-Thege út 29-33, Budapest, Hungary
[b] International Research Center for Renewable Energy (IRCRE), State Key Laboratory of Multiphase Flow in Power Engineering (MFPE), Xi'an Jiaotong University, Xi'an, Shaanxi 710049, China
[c] University of Szeged, Interdisciplinary Excellence Centre, Department of Applied and Environmental Chemistry, H-6720, Rerrich Béla tér 1, Szeged, Hungary
[d] Centre for Energy Research, Institute of Technical Physics and Materials Science, H-1121, Konkoly-Thege út 29-33, Budapest, Hungary

ARTICLE INFO

Keywords:
Fe-complex
$BiVO_4$ semiconductor
Solar water splitting
Photoelectrochemical water oxidation

ABSTRACT

Photoelectrochemical water splitting can become efficient by grafting co-catalysts on semiconductors that improve the interfacial oxygen evolution reaction. We applied a simple non-noble metal pre-catalyst, $[Fe^{II}(PBI)_3]^{2+}$ (PBI is 2-(2′-pyridyl)benzimidazole ligand) for this purpose on a nanopyramidal $BiVO_4$ semiconductor that was morphologically optimal for efficient light harvesting, but its performance suffered from V-poor surface recombination sites. The $[Fe^{II}(PBI)_3]^{2+}$ *in situ* transformed to α-Fe_2O_3 nanoparticles on V-vacant areas of $BiVO_4$ mending their photocurrent-limiting effect. Photoelectrochemistry at pH 8.2 confirmed that the α-Fe_2O_3 co-catalyst improved the charge transfer efficiency by an order of magnitude, suppressed the recombination in the bulk and reduced the charge transfer resistance. Overall, the α-Fe_2O_3 suppressed the recombination on the V-poor surface, while at high potentials it provided high-valent centers for the oxygen evolution. The resulting photocurrent density far exceeding that of $BiVO_4$ or samples modified by $FeCl_3$ or $Fe(NO_3)_3$ underlines the metallochaperone-like effect of the PBI ligand.

1. Introduction

The hourly solar energy influx to earth could almost cover the global annual energy demand [1]. Photoelectrochemical (PEC) water splitting could be an efficient way to capture and store this energy in pure solar hydrogen. However, each step of the photon-to-fuel process must be understood and improved in efficiency in order to overcome the undeniable limitations of the PEC method. These steps are absorption of photons, separation and transfer of photoinduced charge carriers to the surface, hole transport at the surface, and the kinetics of the chemical reactions that all have to take place highly efficiently to not limit the overall performance. However, foremost the complex kinetics of the oxygen evolving reaction (OER) means the bottleneck of the process, thus most of the efforts aim the development of highly efficient photoanodes.

Among metal oxide semiconductors bismuth vanadate ($BiVO_4$) has emerged as a promising photoanode for PEC applications [2–12] due to a suitable bandgap, proper band edge position and low cost. On the other hand, the partial visible light response, high bulk and surface charge recombination, poor electrical conductivity, and slow surface hole transfer kinetics limit the theoretical photocurrent density of ~7.5 mA cm^{-2}, corresponding to a solar-to-hydrogen conversion efficiency (η_{STH}) of ~9.2 % under standard AM 1.5 G sunlight radiation [13]. Smart nanostructures can help overcome the charge carrier transport limits, but in practice, the performance lags far behind the theoretical values due to defect sites. Convenient, low-cost and scalable thin film synthesis of pyramidal-shaped $BiVO_4$ nanowire arrays on photoanodes has been successfully carried out by a facile surfactant-free seed-mediated method [14]. The precise morphology control could be achieved by a stoichiometric ratio of Bi and V precursor salts and thermal annealing to reach high crystallinity. However, these conditions were linked to V-vacancy strongly limiting the photooxidation performance of

* Correspondence to: Centre for Energy Research (CER), KFKI Campus, H-1121, Konkoly-Thege Miklós út 29-33, Budapest, Hungary.
E-mail address: timea.benko@ek-cer.hu (T. Benkó).

https://doi.org/10.1016/j.apcata.2023.119035
Received 9 November 2022; Received in revised form 16 December 2022; Accepted 10 January 2023
Available online 13 January 2023

$BiVO_4$ photoanodes for water splitting [15].

In general, boosting the photooxidation by $BiVO_4$ is viable by different strategies, but most of these would be unsuitable for the morphologically favorable pyramidal $BiVO_4$ nanowire arrays. Heteroatom or defect doping [16,17], and creating hetero- or homo-junctions can overcome drawbacks and facilitate charge separation and transport [18–20]. The most relevant example is a hetero-type dual photoanode consisting of two separate substances – Ti-doped α-Fe_2O_3 and a NiOOH/FeOOH/H_2 treated Mo doped $BiVO_4$ –, instead of combining them in a top-bottom heterojunction arrangement. With this strategy, a photocurrent density of 7.0 ± 0.2 mA/cm^2 at 1.23 V_{RHE} could be achieved in water oxidation under 1 sun illumination [18].

FeOOH also has a beneficial effect on the PEC performance of $BiVO_4$. The amorphous (α-FeOOH) [21] and gamma iron oxyhydroxides (γ-FeOOH) have been effectively coupled to $BiVO_4$ photoanodes. Layers of γ-FeOOH grown by a novel photodeposition method from $FeCl_2$ in a 0.1 M solution revealed a 500 mV cathodic shift in the photocurrent onset potential. Furthermore, an increased photocurrent of 1.0 mA/cm^2 was obtained at a potential of 0.5 V_{RHE}. The FeOOH overlayer on the $BiVO_4$ photoanode prevented the photocorrosion of the electrode, thus improving stability [22]. Even better performance was observed when two catalyst layers of FeOOH and NiOOH were applied on $BiVO_4$ [23–27]. The role of FeOOH at the $BiVO_4$/FeOOH interface correlated to the reduction of the surface recombination and passivating of the $BiVO_4$ surface traps, while the NiOOH at the FeOOH/NiOOH interface made the flat band potential more negative and the kinetics of OER faster [23].

NiFe-(oxy)hydroxide/borate WOC was also applied to the $BiVO_4$ to improve PEC water splitting under front-illumination. The catalyst was co-deposited from a pH 9.5 borate buffer containing Fe(II)- and Ni(II) acetate at 0.6 V_{RHE} under solar irradiation. The resulting $BiVO_4$/$NiFeO_x$-B electrode exhibited a notable photocurrent of 3.2 mA/cm^2 at 0.6 V_{RHE} [28]. Shaddad et al. [29] tested Fe_2O_3, ZrO_2, and Fe_2O_3-ZrO_2 nanoparticle-modified $BiVO_4$ photoanodes and demonstrated a five-fold increase in photocurrent at 1.23 V_{RHE} in the case of Fe_2O_3-ZrO_2/$BiVO_4$, and somewhat lower using Fe/$BiVO_4$. PEC measurements in the presence of a hole scavenger showed the same photocurrent for all samples, therefore the photocurrent improvements could be connected to surface catalysis.

An ultrathin α-Fe_2O_3 layer was also deposited on $BiVO_4$ *via* the spin-coating-based successive ionic layer adsorption and reaction (SILAR) method. The photoanode exhibited improved charge recombination properties due to efficient hole transfer to the surface. The Fe_2O_3/$BiVO_4$ electrode demonstrated 2.14 times higher photocurrent density at 1.23 V_{RHE} under solar illumination and three times higher IPCE values compared to the pristine $BiVO_4$ [30]. A coating of ultrathin, highly crystalline *β*-FeOOH overlayer was growing on a $BiVO_4$ photoanode by a solution impregnation method. This photoanode exhibited doubled photocurrent density than the amorphous FeOOH coated $BiVO_4$ prepared by electrodeposition. This enhanced performance was assigned to the ultrathin crystalline structure of FeOOH and increased oxygen vacancies, which could facilitate the hole transport/trapping and supply more active sites for water oxidation [31].

Further, rather suitable for morphology-preserving improvements become possible by grafting water oxidation catalysts (WOCs) on $BiVO_4$ to improve the sluggish water oxidation kinetics at the surface, thereby reducing the overpotential for the PEC process. In general, co-catalysts can suppress the surface charge recombination by passivation, enhance the water oxidation kinetics, and improve the charge separation efficiency by influencing the band bending of the light-harvesting semiconductor. However, the role of WOCs as co-catalysts in the process often remains unclear. Most authors assume that a WOC exerts its effect by improving water oxidation kinetics [32], while others hypothesise that it has a passivating effect and reduces surface recombination [33].

Nevertheless, typical WOCs have been combined with $BiVO_4$, such as cobalt phosphate (Co-Pi), nickel borate, manganese phosphate [34], RuO_x [35], FeOOH and NiOOH [23], NiMn layered double hydroxide [36] and molecular catalysts such as Ru, Ir, Ni, Co and Fe complexes [37]. Due to the differences in co-catalysts, stable and highly efficient systems demanded various deposition strategies. Co-Pi has been extensively investigated as a co-catalyst on many semiconductors – including $BiVO_4$ – since it was first reported by the Nocera group in 2008 [34,38–41]. The Co-Pi was successfully deposited on the photoinduced surface holes by the photo-assisted electrodeposition method leading to increased hole utilization efficiency by collecting holes.

Zachäus and co-workers concluded about Co-Pi on $BiVO_4$ that despite being a dark electrocatalyst, Co-Pi did not affect the kinetics of OER on the surface of $BiVO_4$ but instead, suppressed surface recombination [35]. Their conclusion was that Co-Pi passivated the surface of $BiVO_4$ rather than catalyzed the OER, as the hole transfer from $BiVO_4$ to the Co-Pi layer is too slow to effectively compete with direct water oxidation by $BiVO_4$. In this case, the slow OER kinetics of Co-Pi resulted in the accumulation of Co^{III} states to increase charge recombination instead of Co^{IV} states to catalyze water oxidation. In addition, the typical electrocatalyst RuO_x did not significantly improve the photoactivity of $BiVO_4$ either, suggesting that $BiVO_4$ by itself is already thermodynamically active towards water oxidation.

Molecular catalysts – such as Ru- [42], Ir- [43], Co- [44–51], Ni- [52,53] and Ni-Fe- [54] complexes – were also coupled with $BiVO_4$ to enhance the photocurrent. In general, higher photocurrent and lower overpotential were indeed reported with the molecular catalyst modified $BiVO_4$ photoanodes, but there is no agreement about the main role of the catalyst. The function of the molecular complex itself seems to depend strongly on the reaction conditions. Some catalysts were reported to suppress charge recombination on the surface; others increased the rate of OER or enhance the charge separation efficiency. In addition, catalyst leaching from the surface and mineralization have been realized as common problems.

Despite the successes achieved with metal-oxide or molecular complex co-catalysts, the true nature of the improvements often remains unclear. Considering that a photoanode may not necessarily operate at a constant potential under realistic conditions, the possible potential-dependence of the co-catalyst effect should also be of interest. Clearly, further studies are required to reveal the precise role of co-catalysts on semiconductor surfaces.

Lastly, a number of the modifications listed above would be hard to carry out at a larger scale, in practice. In this work, we prepared nanopyramidal-shaped $BiVO_4$ film [14,43] and modified it with an earth-abundant iron-based pre-catalyst, $[Fe^{II}(PBI)_3](CF_3SO_3)_2$, that is *tris*[2-(2′-pyridyl)benzimidazole]iron(II) trifluoromethanesulfonate, which is readily prepared and shows high electrocatalytic activity and stability in water oxidation [55]. To demonstrate the practical advantage of the metallochaperone-like hydrophobic PBI ligand in contrast to some iron salt precursors, the drop-casting method was used to immobilization on undoped $BiVO_4$. We investigated the modified $BiVO_4$ photoanode in PEC water oxidation, with special respect to the charge separation, transport and transfer properties of the best performing Fe-PBI derived system at different potentials. We identified the true co-catalyst as hematite nanoparticles by means of several methods and surface analysis techniques, to be detailed herein.

2. Materials and methods

2.1. Materials

Acetonitrile, D_2O, Na_2SO_3, Na_2SO_4, $FeCl_3$, $Fe(NO_3)_3$, $Na_2B_4O_7 \bullet 10H_2O$ and H_3BO_3 were purchased from commercial sources and used without further purification. $Fe(CF_3SO_3)_2$ was purchased from Strem Chemicals. The ligand, 2-(2′-pyridyl)benzimidazole (PBI) was purchased from Sigma-Aldrich, the complex *tris*[2-(2′-pyridyl)benzimidazole]iron(II) trifluoromethanesulfonate (**Fe-PBI**) was synthesised according to a known procedure [56]. Nanopyramidal **$BiVO_4$**

photoanodes were prepared on fluorine-doped tin oxide (FTO) glass substrate, according to a previous work [43].

2.2. Photoelectrochemical experiments

PEC tests were carried out under argon atmosphere. Linear sweep voltammetry (LSV), electrochemical impedance spectroscopy (EIS) and chronoamperometry (CA) were performed on a BioLogic SP-150 potentiostat. The neat and modified $BiVO_4$ anodes were set as working electrodes in a three-electrode arrangement with Pt auxiliary and Ag/AgCl reference electrodes. PEC experiments were performed under irradiation using a Xe lamp (Asahi spectra MAX-303) with an incident light intensity set at 100 mW/cm^2. Sulfite oxidation was studied in a 0.2 M borate buffer at pH 8.2 with 0.5 M Na_2SO_3 as a hole scavenger. Water oxidation measurements were carried out in a 0.2 M borate buffer at pH 8.2. The measured potential (E_{WE}) *versus* Ag/AgCl reference electrode was converted to the reversible hydrogen electrode (RHE) by the Nernst equation: $E_{RHE} = E_{WE} + 0.059\ pH + E_{Ag/AgCl}$, where E_{RHE} is the converted potential against RHE and $E_{Ag/AgCl}$ is 0.197 V at 25 °C.

The O_2 evolution was measured by a Shimadzu GC 2010 Tracera gas chromatograph equipped with a BID detector. Samples were taken from the headspace of an air-tight cell, initially sealed under air instead of inert gas to avoid positive error caused by possible external air leakage. The carrier and the plasma gas were 6.0 He. The in- and outlet pipes were connected to a homemade loop, including an injector unit, a circulating micro-pump, and a 4-stand valve to fill the loop with He gas. The samples were injected into the gas-tight loop and analysed by GC. Calibration of the setup for sample volume and component sensitivity was done by using He gas and artificial air of known composition. The instrument settings were as follows: 50 mL/min total flow rate, 40 mL/min DCG flow rate, 3 mL/min purge flow rate, $T_{column} = 35$ °C, $T_{detector} = 250$ °C.

Electrochemical impedance spectroscopy (EIS) was performed in the potential range of 1.1–1.5 V_{RHE} to obtain the Nyquist plots in a 0.5 M Na_2SO_4 aqueous solution under 100 mW/cm^2 irradiation in the range of 330–600 nm. A model circuit fitted to the experimental data points by using the Z-fit BioLogic software and contained a solution resistance (R_S) and two embedded RQ elements: the capacitance of the space charge layer (Q_{sc}), the charge transfer capacitance (Q_{ct}) and the corresponding resistance of the space charge layer (R_{sc}), and the charge transfer (R_{ct}). This circuit has been used frequently to fit semiconductor-based systems under OER conditions and it was the simplest model to fit reasonably well our experimental data. The Q (constant phase element) represents the inhomogeneity on the surface that causes non-ideality of the double-layer capacitance at the solid/electrolyte interface. In Q, the pre-exponential factor represents the extent of a non-ideal capacity for the constant phase element and the exponent n, which is an ideality factor ranging from 0.5 to 1.

Incident photon to current efficiency (IPCE) was calculated from Eq. (1),

$$IPCE\% = \frac{1240(\text{eV nm}) j_{ph}(mA/cm^2)}{P_{light}(mW/cm^2)\lambda(\text{nm})} 100\% \quad (1)$$

,where j_{ph} is the photocurrent density, P_{light} is the light output at a λ wavelength.

The maximum photocurrent expected at 100 mW/cm^2 was estimated by integrating the photocurrent densities calculated in the appropriate wavelength range according to Eq. (2), presuming that 100 % of the incident light is converted to photocurrent.

$$J_{max} = \int_{\lambda_i}^{\lambda_j} \frac{P_{light}\lambda}{1240} d\lambda \quad (2)$$

,where the J_{max} is the maximum photocurrent, 3.94 mA/cm^2 in our system, P_{light} is the light output at a λ wavelength.

J_{max} achieved with a semiconductor is limited by the absorption efficiency (η_{abs}), the charge separation and transport efficiency in the bulk to the surface (η_{sep}), and the charge transfer efficiency from the surface to the electrolyte (η_{ct}). In a given system, the available photocurrent (J) is determined by these efficiencies: $J = J_{max}\ \eta_{abs}\ \eta_{sep}\ \eta_{ct}$.

The absorption efficiency of the samples was calculated by $\eta_{abs} = 100\ \%$ - R % -T %, where R % is reflectance, T % is transmittance. In the presence of a hole scavenger, the photocurrent is described by $J_{sulfite}/J_{max} = \eta_{abs}\ \eta_{sep}$, where $J_{sulfite}$ is the photocurrent density for sulfite oxidation, J_{max} is the expected maximum photocurrent. The charge transfer efficiency of a photoanode was calculated by $\eta_{ct} = J_{water}/J_{sulfite}$.

2.3. Physical characterization methods

Ultraviolet-visible diffuse reflectance spectrum (UV–vis DRS) was recorded using a Cary 60 UV–vis spectrophotometer (Agilent Technologies Inc., USA) equipped with a lab sphere diffuse reflectance accessory.

In order to determine surface compositions of the electrodes, X-ray Photoelectron Spectroscopy was performed on two different systems: a Specs XPS instrument (equipped with an XR50 dual anode X-ray source and a Phoibos 150 hemispherical electron analyzer), and a Kratos XSAM 800 XPS instrument with an unmonochromatized Al Kα source (1486.6 eV). For the measurement, the samples were cut into 1 × 1 cm sections on a laboratory glass cutting table which were attached to stainless steel sample holders *via* conductive double sided carbon tape. Data were collected in fixed analyzer transmission (FAT) mode at 40 eV pass energy and 0.1 eV step size, and Fe 2p, O 1s, Sn 3d, N 1s, C 1s, V 2p and Bi 4f high resolution spectrum regions were collected for all samples. The aliphatic component of the C 1s spectrum region at 284.8 eV binding energy was used as a reference for charge compensation. The surface ratios of the elements were calculated from the integral intensities of the XPS peaks using manufacturer provided relative sensitivity factors based on Scofield cross sections.

Scanning Electron Microscopy (SEM) investigations of the samples were done on a Thermo Scientific Scios2 (Waltham, MA, USA) dual-beam system equipped with an Oxford X-maxN 20 SDD EDX (Abingdon, UK), 5 keV beam energy and process time 6 were applied, dead time was below 50 %.

The morphology and microstructure of the samples were investigated by Transmission Electron Microscopy (TEM) in HRTEM and HAADF modes using an FEI Titan Themis 200 kV spherical aberration (Cs) - corrected TEM with 0.09 nm HRTEM and 0.16 nm STEM resolution. The composition of the samples was measured by STEM-EDS and elemental maps were obtained by spectrum imaging with 4 Thermofischer "Super X G1″ EDS detectors built in the microscope. Cross sectional lamellae for TEM investigation were prepared by Focussed Ion Beam (FIB) technique in the Scios 2 scanning electron microscope.

Raman spectroscopy survey spectra of the different $BiVO_4$ samples was collected by using an Innovative Photonic Solution laser source (532 nm, >50 mW output power) coupled to an Ocean Optics QEPro spectrometer through a fiber optic Raman probe. Ten collected spectra with 1 s integration time were averaged by the software for each sample. Raman microscopy was carried out by a WiTec Alpha equipment, using a laser excitation at 532 nm, 1.5 mW power, 3 s integration time and 100 × objective.

X-ray diffraction (XRD) measurements were performed using a D8 Discover (Bruker AXS, Karlsruhe, Germany) diffractometer equipped with Göbel-mirror and a scintillation detector with Cu Kα (λ = 1.5406 Å) radiation. The X-ray beam dimensions were 1 mm * 5 mm, the 2Θ step size was 0.02°, scan speed 0.2°/ min. We used the Diffrac.EVA program and the ICDD PDF database for phase identification.

2.4. Preparation of the photoanodes

Pyramidal-shaped $BiVO_4$ was prepared on an FTO coated glass

substrate according to previous works [43]. The special morphology was advantageous for catalyst deposition due to the large surface area and extended electronic properties [57]. In our earlier study [55], the **Fe-PBI** pre-catalyst complex in Fig. 1 resulted in excellent electrocatalytic performance under heterogeneous conditions in OER. Therefore, in this work, the **$BiVO_4$** photoanode was modified with **Fe-PBI** dissolved in acetonitrile, by a simple drop-casting method that allowed a very low surface concentration of 8 nmol/cm^2. The **Fe-PBI** was dissolved in acetonitrile in 6 mM concentration. In a typical experiment, a 100 μL aliquot of the solution was drop-casted onto **$BiVO_4$** using a micro-syringe. Acetonitrile was evaporated at room temperature, and the sample was dried by an infrared lamp for 30 min. The same procedure was followed to prepare **$FeCl_3$/$BiVO_4$** and **$Fe(NO_3)_3$/$BiVO_4$** as references. First, we investigated the effect of the **Fe-PBI** co-catalyst on the charge transfer, surface passivation and recombination processes of the pristine **$BiVO_4$**. The structure and photoelectrochemical performance of the **Fe-PBI/$BiVO_4$** electrode were then compared with the **$FeCl_3$/$BiVO_4$** and **$Fe(NO_3)_3$/$BiVO_4$** electrodes as references to demonstrate the advantages of using the iron-complex.

3. Results and discussion

3.1. Effect of Fe-PBI on the photoelectrochemical properties of $BiVO_4$ photoanode

To calculate the absorption efficiency, the optical properties of the pristine **$BiVO_4$** and **Fe-PBI/$BiVO_4$** were characterized by UV–vis DRS. The samples exhibited similar absorption spectra and the absorption edge was located at *ca.* 500 nm. The corresponding optical band gap energy (E_g) was 2.4 eV for both photoanodes calculated by the Tauc method [58] (Fig. 2a), consistently with literature data [59]. The same E_g values of the samples indicated that the catalyst loading did not change the band structure of **$BiVO_4$** and did not block the light absorption. The η_{abs} reached nearly 90 % between 450 nm and 300 nm at both samples (Fig. 2b) indicating the generation of similar amount of electron/hole (e^-/h^+) pairs.

Next, we studied the charge separation and transport efficiency, also known as hole collection efficiency, expressing the fraction of the photogenerated holes that reach the surface. The charge separation and transport process during the PEC oxidation reaction were studied in the presence of 0.5 M Na_2SO_3 as a hole scavenger in the electrolyte since the oxidation of sulfite anion is thermodynamically and kinetically more facile than the oxidation of water (Eqs. 3 – 4), so the charge transfer efficiency is assumed to be 100 %.

$$2H_2O + 4h^+ \rightarrow 4H^+ + O_2\ E^o = 1.23\ V_{RHE} \quad (3)$$

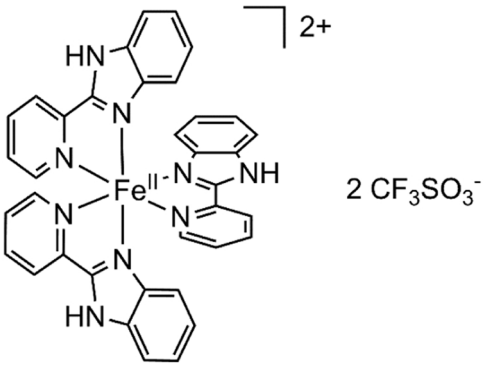

Fig. 1. The water-insoluble [$Fe^{II}(PBI)_3$](OTf)$_2$ (PBI =2-(2′-pyridyl)benzimidazole; OTf− = trifluoromethylsulfonate anion) applied to $BiVO_4$ as pre-catalyst complex. One of the PBI ligands was shown earlier to dissociate from the complex driven by solution chemistry, furnishing the active form of the complex with open sites at cis-positions [55].

$$SO_3^{2-} + h^+ \rightarrow SO_3^- E^o = 0.73\ V_{RHE} \quad (4)$$

Since the separation-transport efficiency depends on the layer thickness, which affects the absorption efficiency, the two parameters can be determined together. Fig. 3a shows the LSV curves of the photoanodes in the presence and absence of sulfite under chopped light irradiation. In the presence of hole scavenger, the pristine **$BiVO_4$** and the **Fe-PBI/$BiVO_4$** showed a photocurrent density of 1 mA/cm^2 and 1.3 mA/cm^2, respectively, at 1.23 V_{RHE}. This increased photocurrent indicated that more holes could be transported to the surface and reacted rapidly with sulfite in **Fe-PBI/$BiVO_4$** than in **$BiVO_4$** [60]. Fig. 3b shows the charge separation efficiency of the photoanodes, η_{sep} as a function of the applied potential. For **$BiVO_4$**, η_{sep} increased from 0 % to 30 % in the applied potential range. The low η_{sep} values can be attributed to high e^-/h^+ recombination in the bulk defect sites, surface traps, or poor electron transport [61]. The introduction of **Fe-PBI** on the surface clearly increases charge separation efficiency from as low potential as 0.1 V_{RHE} (Fig. 3b), possibly due to the presence of surface states.

The charge recombination and trapping processes are more likely due to the high O and V deficiency of the $BiVO_4$. The nanopyramidal surface structure is advantageous in the migration of holes to the surface [62,63], however, the presence of multiple defect states can cause electron trapping. The co-catalyst increased the η_{sep} to 25 % even at 0.6 V_{RHE}, which further improved to 35 % at 1.6 V_{RHE}. The enhanced η_{sep} of **Fe-PBI/$BiVO_4$** compared to **$BiVO_4$** suggested that the added Fe-complex could facilitate the transport of holes to the surface in the applied potential range of −0.1 V_{RHE} to +1.6 V_{RHE}, by blocking defect sites.

The charge transfer efficiency of a photoanode provides information about the fraction of holes transferred from the surface into the electrolyte. Fig. 3c shows the charge transfer efficiency of the photoanodes as a function of the applied potential. Low η_{ct} values were achieved with the pristine **$BiVO_4$**, but in the case of **Fe-PBI/$BiVO_4$** the η_{ct} was considerably higher in the applied range, showing a 16-fold increase at 1.23 V_{RHE}. The η_{ct} expresses kinetic competition between charge transfer and surface recombination illustrated by the photocurrent transients in Fig. 3d. In the case of pristine **$BiVO_4$**, after switching on the light, a fast decrease in photocurrent can be observed as a result of the surface e^-/h^+ recombination. When the light is off, the holes recombine with the free electrons in the conduction band, involving electron withdrawal from the external circuit, which explains the transient cathodic current.

Modification of the **$BiVO_4$** with **Fe-PBI** changed the transient profile of the photocurrent. When the light is on, a higher initial photocurrent is generated, which means that more surface holes can be involved in the oxidation of water and the photogenerated charges can exist longer due to the co-catalyst on the surface [42]. In the presence of sulfite, the prompt reaction allows for even more efficient utilization of holes, as shown by the higher initial photocurrent and the absence of current spike. The slow water oxidation reaction results in holes accumulating near the surface, which increases the chance of recombination with electrons and possibly causing photocorrosion, too [64].

The charge transfer resistance (R_{ct}) provides more information about the inhibition of the electron transfer step of the reaction at the interface, which was investigated by EIS. The experiments were performed in 0.5 M Na_2SO_4 in the potential range of 1.1–1.5 V_{RHE} under irradiation. Fig. 4a shows the Nyquist plot and fit of the experimental data based on an equivalent circuit consisting of the two observed semicircles. The first semicircle developing in the high frequency region is attributed to R_{sc} and Q_{sc}, and the second semicircle in the low frequency region is assigned to R_{ct} and Q_{ct}. The semicircles deviate from perfect ones indicating non-ideal behavior due to surface irregularities and complexity in the double-layer structure expected for such nanostructured systems [65]. Therefore, the use of Q_{sc} and Q_{ct} is justified instead of ideal capacitors.

Fig. 4b shows the charge transfer resistances in the function of the applied potential. The charge transfer resistance of both photoanodes

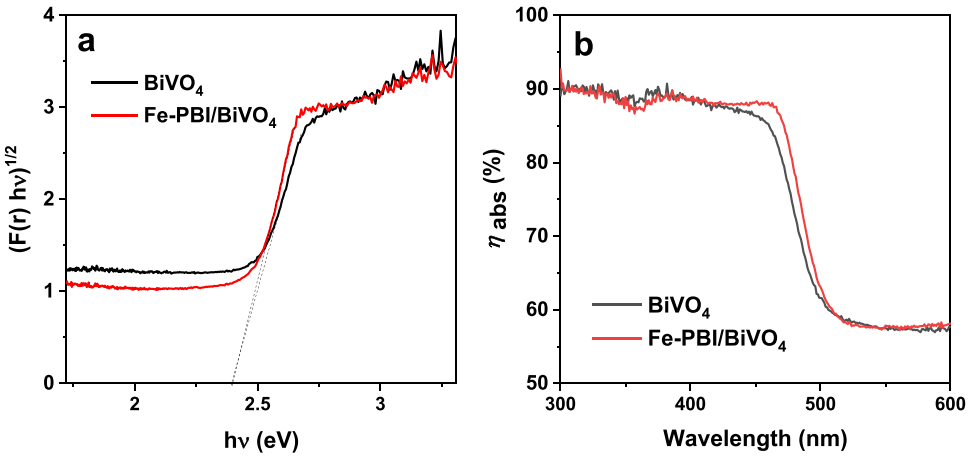

Fig. 2. a) The Tauc plot and (b) the corresponding absorption efficiency and of **$BiVO_4$** and **Fe-PBI/$BiVO_4$** photoanodes obtained from the UV–visible diffuse reflectance spectra.

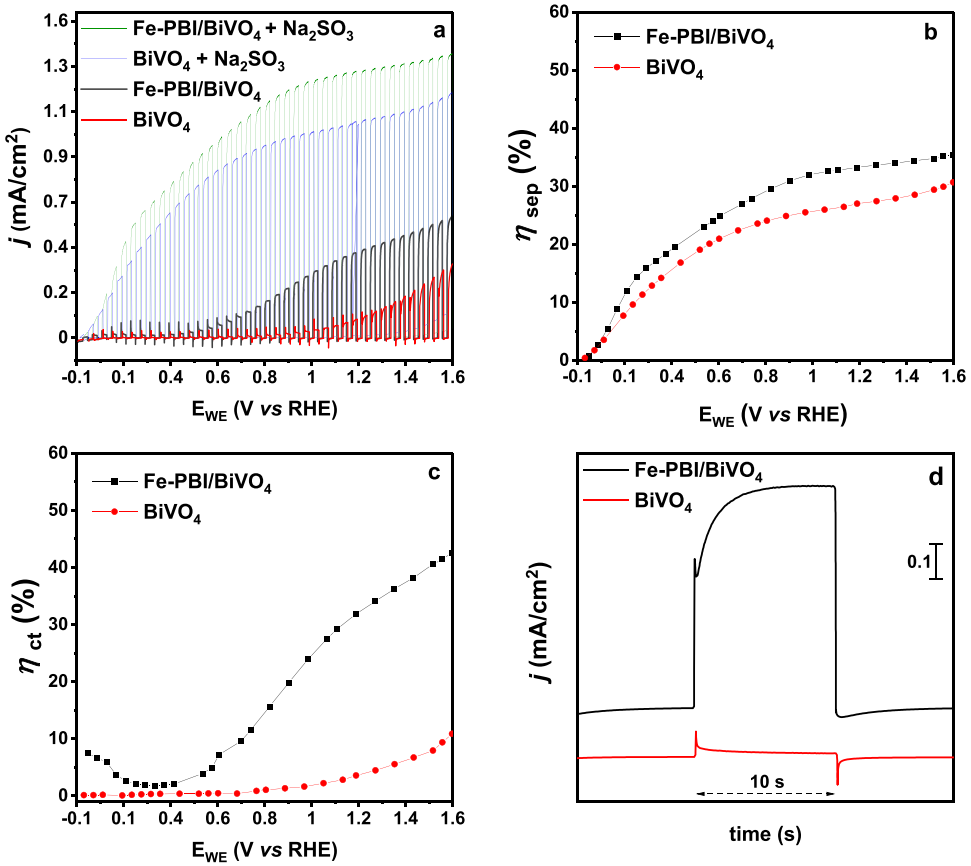

Fig. 3. a) Linear sweep voltammetry plots of **$BiVO_4$** and **Fe-PBI/$BiVO_4$** photoanodes obtained in 0.2 M borate buffer at pH 8.2, in the presence/absence of 0.5 M Na_2SO_3 under chopped irradiation with 100 mW/cm^2, $\nu = 2$ mV/s, Pt aux. and Ag/AgCl ref.); b) charge separation (η_{sep}) and c) charge transfer (η_{ct}) efficiency of the **$BiVO_4$** and **Fe-PBI/$BiVO_4$** photoanodes; d) comparison of photocurrent transients measured at 1.23 V_{RHE} under chopped irradiation with 100 mW/cm^2, 0.5 M Na_2SO_3 was used where indicated.

decreased as the potential and the degree of band bending increased. Accordingly, the photogenerated holes can overcome the energy barrier at higher potentials to react more effectively with water. As the rate of water oxidation increased, the surface charge recombination dropped. At higher applied potentials, the passivation of the surface states does not play a role [42].

The difference between the R_{ct} values of the photoanodes decreased with anodic polarization (Fig. 4b) suggesting that the co-catalyst has less effect on surface recombination at higher potentials. On the other hand, the difference in charge transfer efficiency of the **$BiVO_4$** and **Fe-PBI/$BiVO_4$** photoanodes remained large at those potentials (Fig. 3 c). This apparent contradiction suggests that charge transfer prevails over charge recombination at higher potentials. The charge transfer can take place at the electrode/electrolyte interface and the semiconductor/co-catalyst interface, that is, at the catalytic centers.

At lower potentials, the **Fe-PBI/$BiVO_4$** photoanode showed much lower R_{ct} than pristine **$BiVO_4$**, indicating suppressed charge recombination and thus promoting OER. On **$BiVO_4$**, the first step of OER is the adsorption of the water molecules on O vacancies in the uppermost layer [66]. In addition to these oxygen-deficient sites, **Fe-PBI/$BiVO_4$** also provides high-valent Fe states at surface sites, which are known to be highly active reaction centers for water molecules, resulting in more efficient use of holes reaching the surface [63]. Those holes can be involved in the OER or recombine at surface states due to the high

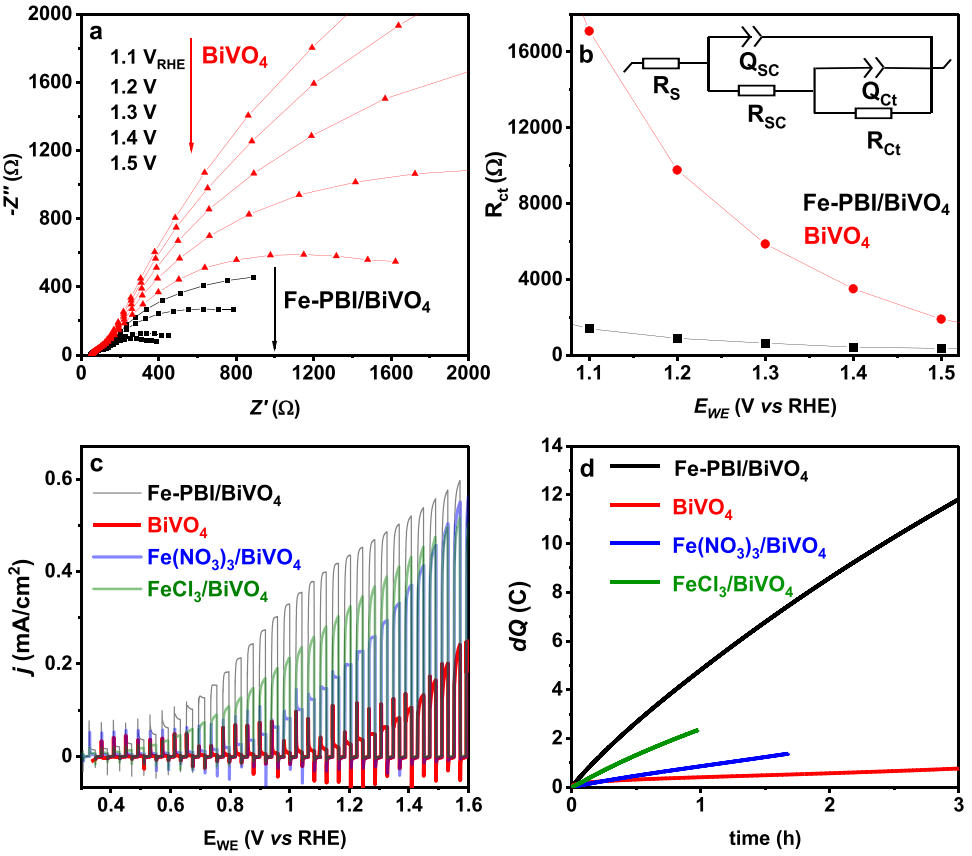

Fig. 4. a) Nyquist plots and fit of the experimental data and b) the charge transfer resistance (R_{ct}) of **BiVO$_4$** and **Fe-PBI/BiVO$_4$** photoanodes based on an equivalent circuit (see the inset) as a function of the applied potential obtained in 0.5 M Na_2SO_4 under 100 mW/cm^2 irradiation in the range of 330–600 nm; c) linear sweep voltammetry of **BiVO$_4$** and **Fe-PBI/BiVO$_4$** photoanodes measured in 0.2 M borate buffer at pH 8.2, under chopped light irradiation with 100 mW/cm^2 in the 330–600 nm range at ν of 2 mV/s, Pt aux. and Ag/AgCl ref. electrode; d) the passed charge during controlled potential electrolysis with **BiVO$_4$** (red), **Fe-PBI/BiVO$_4$** (black), **FeCl$_3$/BiVO$_4$** (green) and **Fe(NO$_3$)$_3$/BiVO$_4$** (blue) at 1.5 V_{RHE} for 3 h in 0.2 M borate buffer at pH 8.2 under 100 mW/cm^2 irradiation in the range of 330–600 nm. The surface concentration of co-catalysts was 8 nmol/cm^2 for all the **Fe-PBI/BiVO$_4$**, **FeCl$_3$/BiVO$_4$** and **Fe(NO$_3$)$_3$/BiVO$_4$** photoanodes.

kinetic barrier of water oxidation. Iron species with high oxidation states may "store" the holes at the surface, which allow to accelerate OER [63]. Thus, the results suggest that the co-catalyst on **BiVO$_4$** accelerates the kinetics of OER at higher potentials and reduces the surface hole recombination at lower potentials.

3.2. *Photoelectrocatalytic performance of the photoanodes*

The photoelectrochemical properties of the photoanodes were investigated under conditions that ensure optimal performance of **Fe-PBI**. The mild basic pH corresponds to the 7.5–8.4 value of seawater that is a more reasonable source for large-scale utilization in water splitting than sweetwater stocks. LSV experiments were performed on **BiVO$_4$**, **Fe-PBI/BiVO$_4$**, **FeCl$_3$/BiVO$_4$** and **Fe(NO$_3$)$_3$/BiVO$_4$** photoanodes in the potential range of 0.2 V_{RHE} to 1.6 V_{RHE} in a three-electrode electrochemical cell under chopped irradiation (Fig. 4c). The **Fe-PBI/BiVO$_4$** photoanode exhibited a large photocurrent increase compared to **BiVO$_4$**, onset potential of water oxidation shifted cathodically to 0.3 V_{RHE}, which is 0.6 V lower than that of the **BiVO$_4$**. The IPCE improved to a large extent at 1.23 V_{RHE} and 1.78 V_{RHE} (Fig. S1). The **Fe-PBI/BiVO$_4$** showed *ca.* 20-fold increase in IPCE % compared to **BiVO$_4$** at 1.78 V_{RHE} and 430 nm. The performance of the **Fe-PBI/BiVO$_4$** photoanode exceded that of the **FeCl$_3$/BiVO$_4$** and **Fe(NO$_3$)$_3$/BiVO$_4$** photoanodes, too. This phenomenon suggests that the Fe-complex plays a special role in the PEC performance of $BiVO_4$ compared to the iron-salt precursors. The unprecedented increase caused by the WOC component in our system we tentatively associated at this stage with the high number of V-vacant sites that could be effectively amended by **Fe-PBI**.

We also have done experiments at pH 9, both at 0.2 M and 0.5 M electrolyte concentrations (Fig. S2). The results show a somewhat better performance for both **BiVO$_4$** and **Fe-PBI/BiVO$_4$** due to the different ionic bilayer structures that can promote surface charge transfer.

A long-term electrolysis experiment was carried out to test the stability and oxygen-producing ability of **Fe-PBI/BiVO$_4$** in borate buffer at pH 8.2, under 100 mW/cm^2 irradiation. The potential of the **Fe-PBI/BiVO$_4$** working electrode was set to 1.5 V_{RHE}, the electrolyte stirred, and the compartment of the counter electrode separated by Nafion membrane. Gas bubbles were observed shortly, and after 3 h in a closed cell, the evolution of oxygen gas was confirmed by GC analysis of a headspace sample. Fig. 4d and Fig. S3 show the charge in a 3-h CA experiment and the corresponding I-t curves, respectively, that is compared to the almost negligible values for the pristine **BiVO$_4$**. The observed pass of 12 C for **Fe-PBI/BiVO$_4$** corresponds to the production of 31.3 μmol O_2 as the theoretical maximum. Since 18.7 μmol of O_2 was detected by GC from the headspace and 7.6 μmol accumulated in the electrolyte detected with an optical oxygen sensor immersed in the buffer, an overall 84 % Faradaic efficiency, a TON of 1463, and a TOF of 473 h^{-1} can be calculated at an overpotential of 0.3 V ($\eta = E_{WE} + E(\mathrm{Ag/AgCl}) - E^{\circ}(O_2/H_2O) + 0.059$ pH). The TON and TOF values were calculated considering the 8 nmol/cm^2 initial **Fe-PBI** surface concentration, since the pristine **BiVO$_4$** produced only a negligible amount of O_2, below the detection limit of the GC (Fig. 4d, red curve).

The decrease in the photocurrent densities during the PEC measurement may arise from V leaching or due to photocorrosion originating from hole accumulation on the surface. The dissolution of Fe from the surface can be excluded due to the same Fe/Bi ratio on the surface detected by XPS (*vide infra* in Table 1) on the as-prepared and used **Fe-PBI/BiVO$_4$**. The beneficial effect of utilizing **Fe-PBI** was confirmed by the experiment in which $FeCl_3$ and $Fe(NO_3)_3$ precursors were used on $BiVO_4$ as references [67], since these photoanodes showed markedly lower photocurrent in long-term electrolysis (Fig. 4d).

Further investigating the impact of the co-catalyst on $BiVO_4$, the protium/deuterium kinetic isotope effect (KIE) was studied. This method gives information about the role of proton transfer in the rate-limiting step of a chemical reaction. To avoid problems from surface hole trapping (non-Faradaic current), KIE was determined based on the

Table 1
Surface atomic concentrations (%) of the **$BiVO_4$**, as-prepared and used **Fe-PBI/$BiVO_4$**, the used **$FeCl_3$/$BiVO_4$** and the used **$Fe(NO_3)_3$/$BiVO_4$** photoanodes calculated from XPS data. The used photoanode was tested by CPE at 1.5 V_{RHE} in 0.2 M borate buffer at pH 8.2 for over 3 h.

	$BiVO_4$	Fe-PBI/$BiVO_4$ as-prepared	Fe-PBI/$BiVO_4$ used	$FeCl_3$/$BiVO_4$ used	$Fe(NO_3)_3$/$BiVO_4$ used
Fe	-	0.5	0.6	2.8	2.9
Bi	5.7	6.9	10.7	12.4	13.4
O	39.6	38.9	47.1	46.7	45.9
V	3.4	3.3	3.6	7.7	6.1
N	-	4.0	0.5	0.6	0.6
C	51.3	42.6	37.5	29.9	31.2
F	-	3.7	-	-	-

steady-state photocurrent of CA curves at the oxygen evolution potential after 60 s of irradiation in 0.5 M Na_2SO_4, in D_2O or H_2O [68]. The calculated KIE (J_{H2O}/J_{D2O}) of 2.8 at 1.5 V_{RHE} indicated that protons are involved in the rate-limiting step, while charge transfer from the semiconductor to the co-catalyst is a relatively rapid process.

3.3. Structure and composition of the electrodes

Top-view images by SEM confirmed that the morphology of the **$BiVO_4$** photoanode contained pyramidal $BiVO_4$ blocks (Fig. 5a-b), which were also clearly visible on the side-view TEM images (Fig. 5c-d). In TEM, a Pt-C paste was applied to the surface of the sample to prepare the side-view layer for a better contrast, which is visible as a dark homogeneous part on top of the $BiVO_4$ spikes. The bright patches in the picture indicate the area where the paste could not penetrate. Layers from bottom to top as shown in Fig. 5c are glass substrate, FTO, $BiVO_4$ compact layer and $BiVO_4$ nanopyramid-layer. Fig. 5d shows the magnified image of the pyramid-like structured $BiVO_4$. At the top of the FTO layer, the compact $BiVO_4$ layer is roughly 100 nm in width and the highest spikes are ~250 nm high.

By the XRD analysis of $BiVO_4$ and a used **Fe-PBI/$BiVO_4$** sample, no other phase than $BiVO_4$ could be detected and the reflections of the unmodified and modified samples were fundamentally identical (Fig. S4). This underlines that the V-vacant nature of the samples detected by XPS (Table 1) must be located at the surface, since no crystalline bismuth oxide phase is present according to XRD.

XPS analysis of the as-prepared and used **Fe-PBI/$BiVO_4$** photoanodes indicated Bi, V, O, C, and Fe on the surface of both samples, but N was present only in the as-prepared **Fe-PBI/$BiVO_4$** (Table 1). The surface composition of the as-prepared **Fe-PBI/$BiVO_4$** showed N/Fe ratio close to the expected 9:1, consistent with **Fe-PBI** on the surface. For the used **Fe-PBI/$BiVO_4$**, hardly any N can be found on the surface, suggesting complex decomposition under light irradiation, the Fe content on the other hand was unchanged. Although the same amount of **Fe-PBI** as $FeCl_3$ and $Fe(NO_3)_3$ was applied to $BiVO_4$, the higher Fe/Bi ratio of **$FeCl_3$/$BiVO_4$** and **$Fe(NO_3)_3$/$BiVO_4$** is an indication of uneven surface distribution of the iron species derived from $FeCl_3$. The adventitious carbon is found on the surface of most air-exposed samples, which causes the high C content in our samples. Even short exposures to atmosphere can produce these films, therefore its presence on the **$BiVO_4$** photoanode has no role in the PEC reactivity.

For the as-prepared **Fe-PBI/$BiVO_4$** sample, the Fe 2p binding energies at 723.6 (Fe $2p_{1/2}$) and 709.8 eV (Fe $2p_{3/2}$) (Table 2) with satellite features are typical for high-spin Fe^{2+} or Fe^{3+} (Fig. 6), which is consistent with the **Fe-PBI** complex after one ligand is dissociated [55].

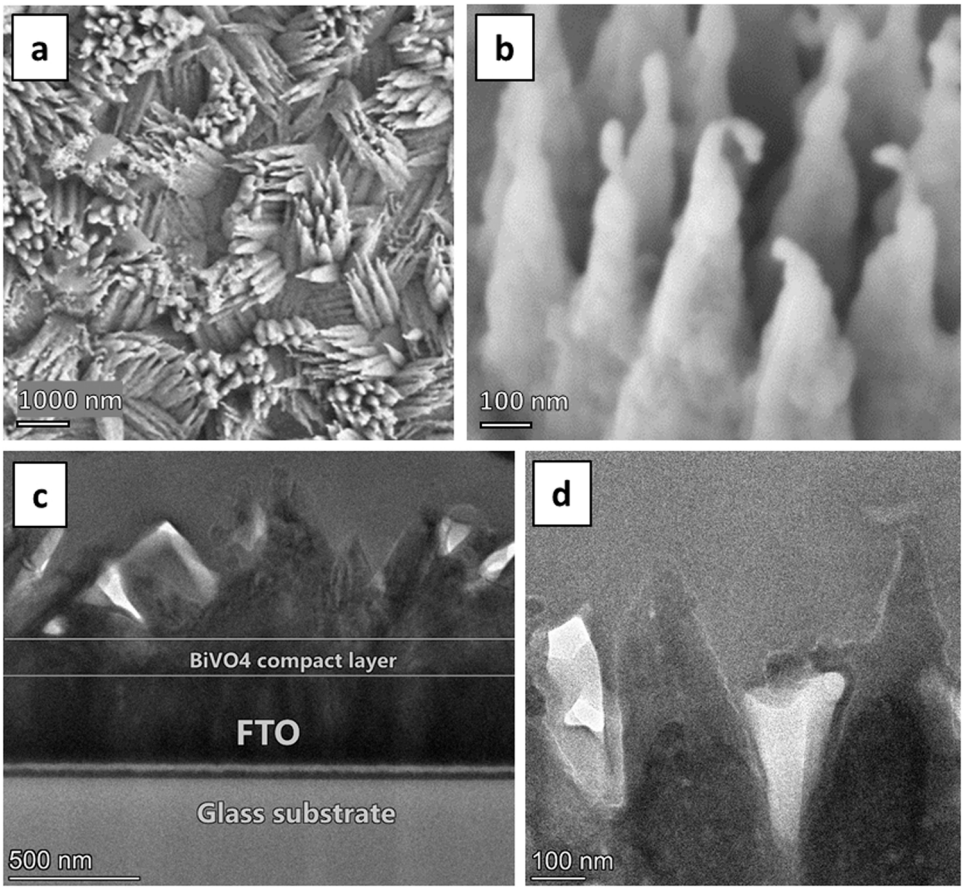

Fig. 5. a) – b) Top-view SEM pictures of the **$BiVO_4$** electrode at × 10,000 and × 100,000 magnifications; c) side-view TEM image of the **$BiVO_4$** photoanode and d) a magnified, side-view TEM image of the same sample. In the images, $BiVO_4$ spikes can be observed.

Table 2
XPS binding energy of the Fe 2p, O 1s, N 1s, V 2p, and Bi 4f photoelectrons of the photoanodes.

	Binding energy (eV)							
	Fe $2p_{3/2}$	Fe $2p_{1/2}$	O 1s			N 1s	V $2p_{3/2}$	Bi $4f_{7/2}$
			$O_{lattice}$	$O_{vacancy}$	H_2O_{ads}			
Fe-PBI/$BiVO_4$ as-prep.	709.8	723.6	529.7	531.7	533.2	399.9	516.6	159.0
Fe-PBI/$BiVO_4$ used	710.8	724.2	529.5	531.2	532.8	399.5	516.4	158.8
$BiVO_4$ used	-	-	529.5	531.7	533.1	-	516.5	158.8
$FeCl_3$/$BiVO_4$ used	710.5	724.4	529.4	531.1	532.5	399.5	516.3	158.8
$Fe(NO_3)_3$/$BiVO_4$ used	711.1	725.0	529.6	531.3	532.9	399.5	516.6	158.8

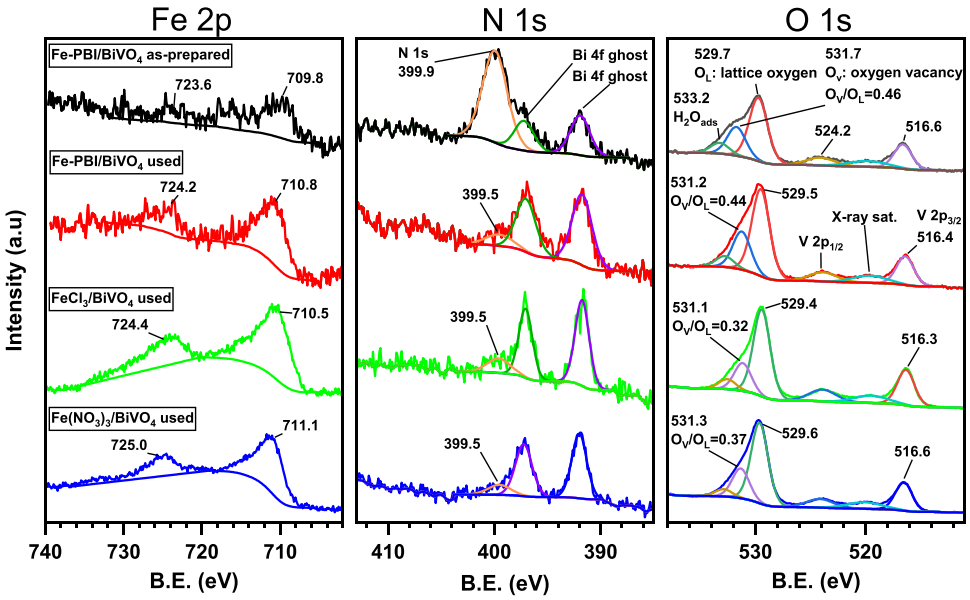

Fig. 6. XP spectra of the as-prepared and used **Fe-PBI/$BiVO_4$**, used **$FeCl_3$/$BiVO_4$** and used **$Fe(NO_3)_3$/$BiVO_4$** photoanodes. The O_V and O_L denote the components corresponding to the oxygen-deficient region and lattice oxygen, respectively.

The dissociation of the first PBI ligand from the tris-chelate precursor in Fig. 1 is likely to take place in acetonitrile solution upon heating that is, under the conditions of drop-casting. For the used **Fe-PBI/$BiVO_4$** sample, the binding energies at 724.2 (Fe $2p_{1/2}$) and 710.8 eV (Fe $2p_{3/2}$) are typical for Fe^{3+}. The Fe^{3+} species can be related to Fe_2O_3 or FeOOH, which refers to complex mineralization considering also the absence of N in the used **Fe-PBI/$BiVO_4$** sample [69,70]. For the **$FeCl_3$/$BiVO_4$** and the **$Fe(NO_3)_3$/$BiVO_4$** samples, the binding energies (Table 2) and the absence of chlorine also indicated the presence of Fe_2O_3 or FeOOH on the surface [71].

The O 1s peaks can be deconvoluted into three components with BEs of 529.7 eV, 531.7 eV, and 533.2 eV. The first component is consistent with lattice oxygen species (O_L); the second can be assigned to the oxygen-deficient region (O_V), which includes different oxygen species (O^- or O_2^{2-}), hydroxyl groups (OH^-), and surface oxygen vacancies. The last peak, at higher energy can be related to surface adsorbed O_2 and/or H_2O [31,60]. Based on the peak areas, the ratios of O_V/O_L were calculated. The O_V content of **$BiVO_4$**, the as-prepared **Fe-PBI/$BiVO_4$**, the used **Fe-PBI/$BiVO_4$**, the **$FeCl_3$/$BiVO_4$** and **$Fe(NO_3)_3$/$BiVO_4$** were 44 %, 46 %, 44 %, 32 % and 37 % respectively. The low activity of the pristine **$BiVO_4$** can be explained by the high O_V/O_L ratio. Generally, defect sites in semiconductors negatively affect their photocatalytic activity due to enhanced charge recombination. However, a moderate amount of vacancy defect can effectively tailor the electronic structure of $BiVO_4$ and increase the conductivity and mobility of charges, hence promoting photocatalytic activity [72].

The V 2p peak corresponded to V^{5+} in each sample, however the presence of V^{4+} cannot be excluded considering that the difference in binding energy is only ~1 eV and the high O_V/O_L ratio of the photoanodes can be correlated with V^{4+}/V^{5+} [73]. The spectra showed a low V/Bi ratio of 0.6 for the used **$BiVO_4$** and **$FeCl_3$/$BiVO_4$**, and a slightly lower ratio of 0.5 for the as-prepared **Fe-PBI/$BiVO_4$** and **$Fe(NO_3)_3$/$BiVO_4$** photoanodes, which can be explained by the inhomogeneity of the $BiVO_4$ samples. In the case of the used **Fe-PBI/-$BiVO_4$**, the V/Bi ratio was significantly lower, 0.3, which may be caused by leaching into the electrolyte during the long-term electrolysis [74]. The surface atomic ratio of V/Bi has been suggested to decrease significantly upon light irradiation, resulting in a bismuth-rich surface and a significant decrease in photocurrent [25].

The Fe 2p spin-orbit coupling values are listed and compared with literature values for some minerals in Table 3. The value for each sample

Table 3
Spin-orbit coupling values for Fe 2p in various iron compounds.

	Fe ΔE ($2p_{1/2}$-$2p_{3/2}$) (eV)	Fe $2p_{3/2}$ B. E. (eV)	Reference
Fe metal	13.1	707.0	[75]
α-Fe_2O_3 (haematite)	13.6	710.9	[75]
α-FeOOH (goethite)	13.5	711.0	[76]
γ-Fe_2O_3 (magheamite)	13.9	710.2	[77]
β-FeOOH (akaganeite)	13.7	711.0	[78]
γ-FeOOH (lepidocrocite)	13.9	710.6	[79]
Fe-PBI/$BiVO_4$ as-prepared	13.8	709.8	This work
Fe-PBI/$BiVO_4$ used	13.4	710.8	This work
$FeCl_3$/$BiVO_4$ used	13.9	710.5	This work
$Fe(NO_3)_3$/$BiVO_4$ used	13.9	711.1	This work

is consistent with a high spin Fe^{3+} state of the co-catalyst content. Considering the ΔE and B.E. values of the used **Fe-PBI/BiVO$_4$**, α-Fe_2O_3 or α-FeOOH was most likely formed from Fe-PBI under irradiation.

SEM images of the photoanodes used in PEC experiments (Fig. 7) confirmed that the pyramidal morphology was preserved. Iron was detected by SEM-EDX by scanning an extended area of the photoanodes, but no distinct surface structures related to iron compounds could be observed in the images. Therefore, well-distributed iron species were assumed for **Fe-PBI/BiVO$_4$** and a less uniform distribution for the **FeCl$_3$/BiVO$_4$** and **Fe(NO$_3$)$_3$/BiVO$_4$** taking into account also the XPS results.

The elemental mapping by TEM-EDX of chosen areas gave information on the distribution of Sn, Bi, V, Pt, O, and Fe. The HAAD image combined with elemental maps (Fig. 8) makes the different layers of the sample more visible. Elemental mapping revealed that the Fe-content detected by XPS originated from the mineralized Fe-complex since no nitrogen was detected. An exemplary, 200 nm size Fe and O containing block in a particular area of the sample is shown in Fig. 8 suggests that the **Fe-PBI** pre-catalyst indeed transformed to Fe_2O_3 or FeOOH nanoparticles (NPs, see also the XPS).

Fig. 9a–d shows HAAD image and the elemental maps of a magnified part of Fig. 8, where Fe has been detected. The atomic distribution along the axis from the top to the bottom of the enclosing rectangle (indicated by red arrows in Fig. 9a−e) and the fractions as a function of the position (Fig. 9e) revealed that the Fe-containing NP was located at the vanadium vacant site at the top of the $BiVO_4$ spike. This specific deposition of the NPs at the apex of the nanopyramids was prompted by the spontaneous photo-electric-field-enhancement effect, which was observed for co-catalysts coupled with pyramidal structured $BiVO_4$ [80,81]. The V vacant areas are clearly visible when comparing Fig. 9b and 9d.

A selective deposition of FeO_x layer has been published starting from an eleven Fe-containing polyoxometalate (Fe_{11}POM) [82]. The Fe_{11}POM was decomposed on the hole-rich 110 sides of the $BiVO_4$ photoanode upon irradiation, while $FeCl_3$ precursor evolved the FeO_x deposition on all facets of the decahedron shaped $BiVO_4$. That facet-selective decomposition of Fe_{11}POM to FeO_x resulted in 5 times higher activity than FeO_x derived from $FeCl_3$. This sort of selectivity explains well the two times higher O_2 production with the **Fe-PBI/-BiVO$_4$** sample than that of the **FeCl$_3$/BiVO$_4$** and **Fe(NO$_3$)$_3$/BiVO$_4$** further, emphasizes the role and importance of the very simple **Fe-PBI** pre-catalyst complex. In addition, our results indicate that the Fe-rich cap on the $BiVO_4$ pyramid contains of Bi, Fe and O in ~0.5: 1: 1 ratio, but lacks V completely. Considering the vastly improved OER activity of **Fe-PBI/BiVO$_4$**, the utilization of water-insoluble first-row transition metal complexes as pre-catalysts is promising. Moreover, such methods may be applied to modify relatively poorly performing, but precisely nano-engineered semiconductors *operando*, in a morphology preserving and directed way that may become a prospective material manipulation method capable of fabricating various heterojunctions.

Since the XPS and TEM measurements did not give conclusive results for the FeOOH or Fe_2O_3 polymorph, a special sample was prepared for Raman spectroscopic measurement by drop-casting **Fe-PBI** onto $BiVO_4$ at a ten times higher concentration and treating with light irradiation to obtain a similar surface structure from the Fe compound. The Raman spectra of the as-prepared and used **FePBI/BiVO$_4$**, **BiVO$_4$** and haematite reference electrodes are shown in Fig. 10a–b. In Fig. 10a, the assigned Raman shifts at 127, 211, 327, 366 and 824 cm^{-1} correspond to the monoclinic $BiVO_4$ phase structure [83]. The bands at 127 and 211 cm^{-1} are consistent with the vibration of the crystalline structure (external mode). The bands at 327 and 366 cm^{-1} are attributed to asymmetrical and symmetrical deformation vibrational modes of the VO_4^{3-}, respectively. The band at 824 cm^{-1} correlates to the symmetrical stretching mode of the V-O bond.

The survey spectrum (Fig. 10b) revealed that the decomposition was not complete at this high surface complex concentration and the Raman peaks of **Fe-PBI** were still present and could be identified by comparison to the as-prepared sample. For the as-prepared **Fe-PBI/BiVO$_4$**, the bands corresponding to the 2-(2′-pyridyl)benzimidazole ligand were as follows: the 574 and 643 cm^{-1} peaks belong to the in-plane and out-of-plane deformational vibrations of the benzene and pyridyl rings, respectively. The peaks at 980, 1007, 1165 and 1450 cm^{-1} can be correlated to the CH in-plane and out-of-plane bending vibrational modes of pyridyl and benzene rings. The peak at 1274 cm^{-1} can be associated with pyridyl CN stretching vibration, at 1499 cm^{-1} with the pyridyl-imidazole ring stretching, and 1383, 1549 and 1608 cm^{-1} correspond to CC stretching vibrations of the pyridyl and benzene rings [84].

However, in the used **Fe-PBI/BiVO$_4$** sample, the additional, pronounced peak at 1326 cm^{-1} propounded the presence of α-Fe_2O_3. Thus, the sample was examined under a high-resolution Raman microscope at 100–1100 cm^{-1} and additional peaks were found correlated to α-Fe_2O_3 at surface areas where the complex decomposed. The bands at 296 and 405 cm^{-1} (Fig. 10a) for the used **Fe-PBI/BiVO$_4$** are characteristic of the α-Fe_2O_3 polymorph and can be assigned to the E_g mode. The peak at 1326 cm^{-1} (Fig. 10b) occurred due to second order scattering process and is specific for two-magnon scattering process in α-Fe_2O_3 which originates from the interaction of two magnons generated on antiparallel close spin sites [85,86]. By comparing the Raman wavenumbers with other polymorphs of Fe_2O_3 or FeOOH, we can confirm the presence of α-Fe_2O_3 in our sample.

3.4. On the decomposition mechanism of the precursor complex

The **Fe-PBI/BiVO$_4$** clearly outperformed the **FeCl$_3$/BiVO$_4$** and the **Fe(NO$_3$)$_3$/BiVO$_4$** photoanodes. In part, this can be explained by the water-insolubility of the pre-catalyst complex **Fe-PBI** that helps to retain the Fe-content at the surface upon oxidative degradation and mineralization to α-Fe_2O_3. However, we wanted to elucidate what conditions are required for the degradation of **Fe-PBI** to α-Fe_2O_3 such as (i) irradiation and photosensitization, (ii) polarization of the photoelectrode and photolysis of the higher oxidation state of the Fe-content, (iii) high energy electron-hole pairs at the surface of the $BiVO_4$, or (iv) a

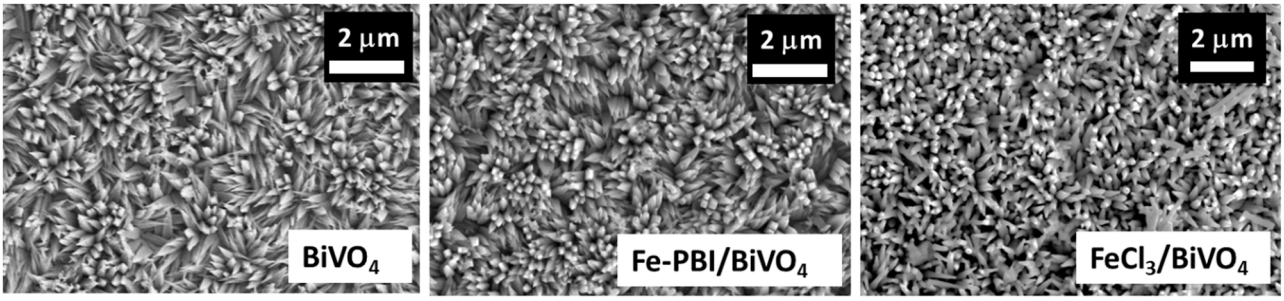

Fig. 7. Top-view SEM pictures of **BiVO$_4$**, **Fe-PBI/BiVO$_4$** and **Fe-Cl$_3$/BiVO$_4$** electrodes at × 10,000 magnifications. The pyramidal morphology of the photoanodes utilized in the PEC experiment was preserved.

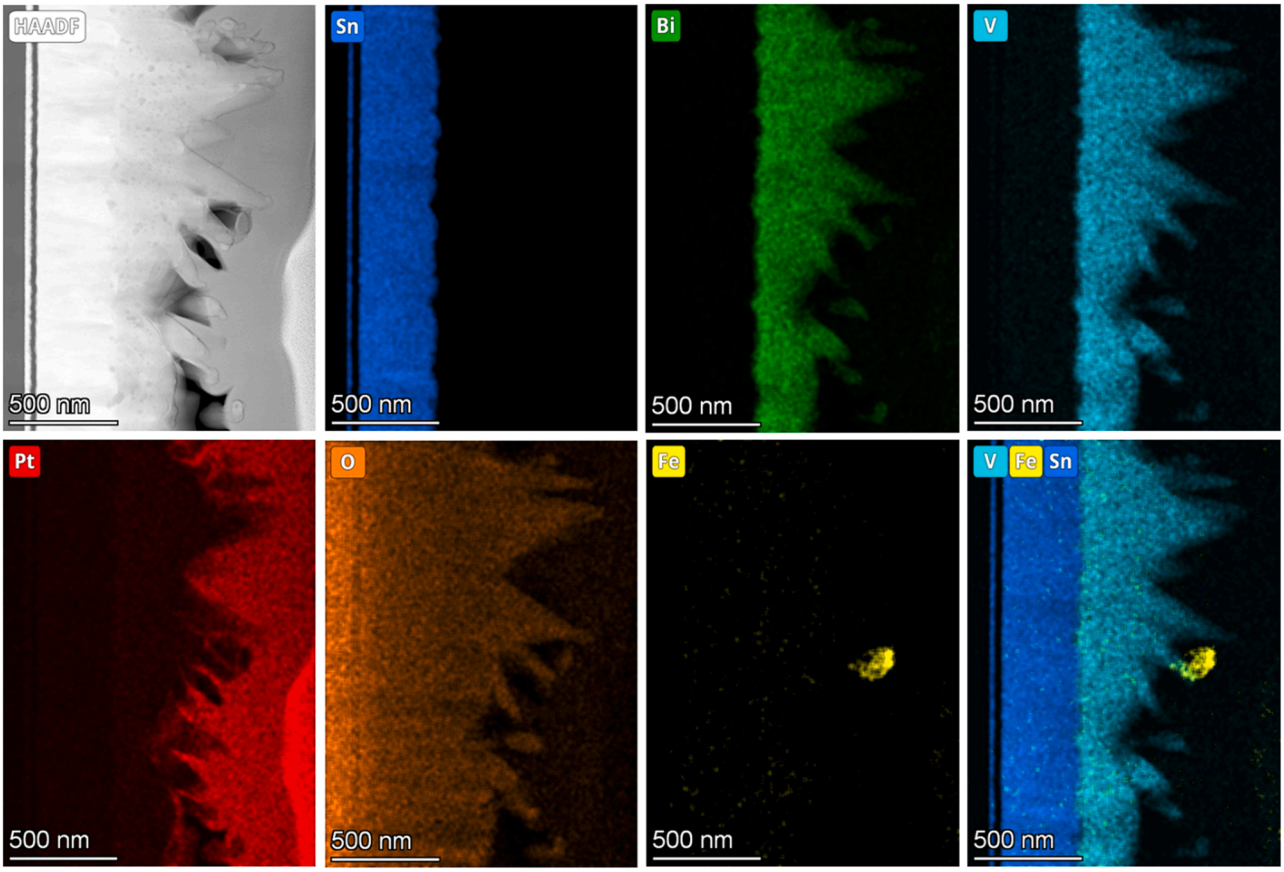

Fig. 8. TEM results of a cross-sectional lamella of the used **Fe-PBI/BiVO$_4$**: HAADF image and elemental mapping of Sn, Bi, V, Pt, O and Fe. A 200 nm size Fe and O containing block is shown at the apex of **BiVO$_4$**.

combination of these. Therefore, we carried out two experiments using **Fe-PBI** drop-casted in 16 nmol/cm^2 concentration to ITO electrodes (three ITO pieces of the same size were modified the same way to enrich the surface in **Fe-PBI** for better detection; one of these was left as-prepared for control).

Previously, the **Fe-PBI/ITO** was found active in water oxidation electrocatalysis (EC) and showed no signs of degradation over *ca.* 200 turnovers in borate buffer at pH 8.3 [55]. The mechanism proposed earlier for the EC process is shown in Fig. 11. If decomposition did not occur and the complex itself participated in the PEC process, these states would presumably occur on the surface.

In the first experiment, **Fe-PBI/ITO** was immersed into borate buffer and irradiated for 1.5 h using the Xe-lamp with a cut-off energy of *ca.* 3.5 eV, see the 'PC hν' route in Fig. 11. This way no electron-hole pairs could be generated in the ITO semiconductor support ($E_g = 3.7$ eV) and only the **Fe^{II}-PBI** was present initially. In the second irradiation experiment, the applied bias of +1.1 V_{RHE} was enough to accumulate the **Fe^{III}-PBI** as the initial state, but it was insufficient to initiate water oxidation (Fig. 11, route 'PEC hν' in the middle.) Finally, it was shown above that the complex is mineralized on $BiVO_4$ at +1.5 V_{RHE} upon irradiation. Under these conditions, the **Fe^{V}-PBI** oxidation state could form in theory and initiate mineralization by surface capturing the high-energy holes of $BiVO_4$.

Follow-up analysis of the two irradiated **Fe-PBI/ITO** samples by means of diffuse reflectance UV–vis spectroscopy, Raman spectroscopy and cyclic voltammetry was performed in order to detect the traces of decomposition of the precursor complex on the ITO surface (Fig. 12). Note that only a minimal physical desorption of the complex occurred from the surface upon sample handling that did not influence the analysis results. The red color of the complex ad-layer changed to red-brown in both cases. Fig. 12a shows the diffuse reflectance spectra of the as-prepared sample (spectrum in black) exhibiting the metal-to-ligand charge transfer (MLCT) band at *ca.* 500 nm typical for **Fe^{II}-PBI** and also the edge of the intra-ligand charge transfer (ILCT) band at $<$ 400 nm for the coordinated PBI [55,56]. For the used samples represented by the spectrum in red (Fig. 12a), the ILCT band for the PBI ligand is drastically lowered and two new bands occur in the 500–700 nm range that are lower in intensity. These bands can be associated with O^{2-}-to-Fe^{III} ligand-to-metal charge transfer (LMCT) typical for oxo-bridged Fe_2^{III} structural features [87–90]. Note that surface-deposited hematite nanoparticles also absorb below 600 nm [91] therefore their presence is also possible according to the UV–vis spectra. Altogether the UV–vis spectroscopic features of the used **Fe-PBI/ITO** samples indicate the loss of a major proportion of PBI and the presence of oxo-bridged high spin Fe^{III} centers.

Raman spectra recorded after the irradiation of both the non-polarized and polarized **Fe-PBI/ITO** exhibit similar features to those of the used **Fe-PBI/BiVO$_4$** shown in Fig. 10b and discussed earlier (Fig. 12b, red spectrum). Importantly, the peak at 1331 cm^{-1} can be directly associated with the formation of α-Fe_2O_3, while the relative intensities of the ligand vibrations – labelled with black numbers to show the Raman shifts – changed drastically. The latter feature suggests again the loss of PBI from the surface, by either dissolution, or degradation and dissolution of the products. Finally, the comparison between the CV scans of as-prepared **Fe-PBI/ITO** (in black) and used **Fe-PBI/ITO** samples (in red) in Fig. 12c also indicate a complete change in the electrochemically active proportion of Fe compound. While the as-prepared **Fe-PBI/ITO** shows the Fe^{III}/Fe^{II} redox that were discussed and established in our earlier work as typical for the **Fe-PBI** complex [55], the used **Fe-PBI/ITO** shows Fe^{III}-to-Fe^{II} reduction below + 0.4 V_{RHE} and re-oxidation that are typical for α-Fe_2O_3 [92–94].

In conclusion – as summarized in Fig. 11 – the **Fe-PBI** is prone to

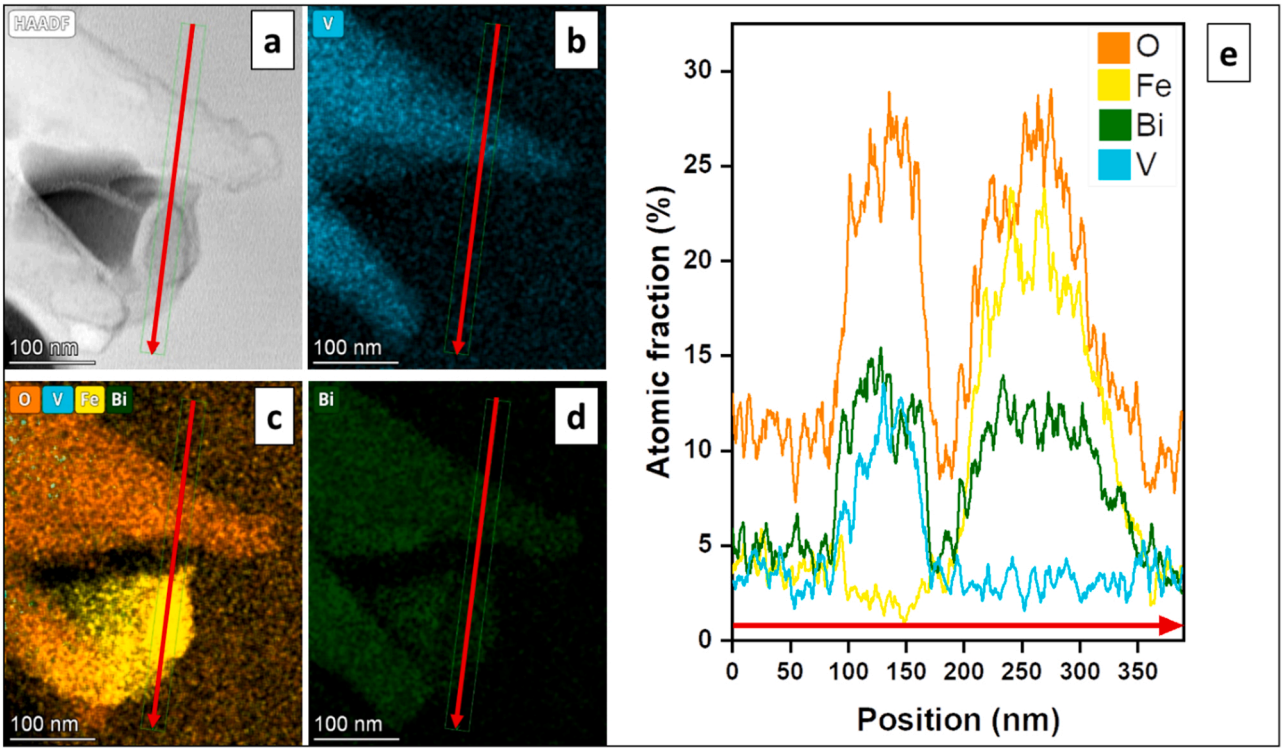

Fig. 9. a) HAAD image and b –d) EDX elemental maps of a magnified part of the image in Fig. 8, of used **Fe-PBI/BiVO$_4$**, where Fe has been detected. The atomic distribution along the axis from the top to the bottom of the enclosing rectangle (indicated by red arrows) and e) the atomic fractions as a function of the position. The Fe-containing NP was located at the vanadium vacant site at the top of the BiVO$_4$ spike.

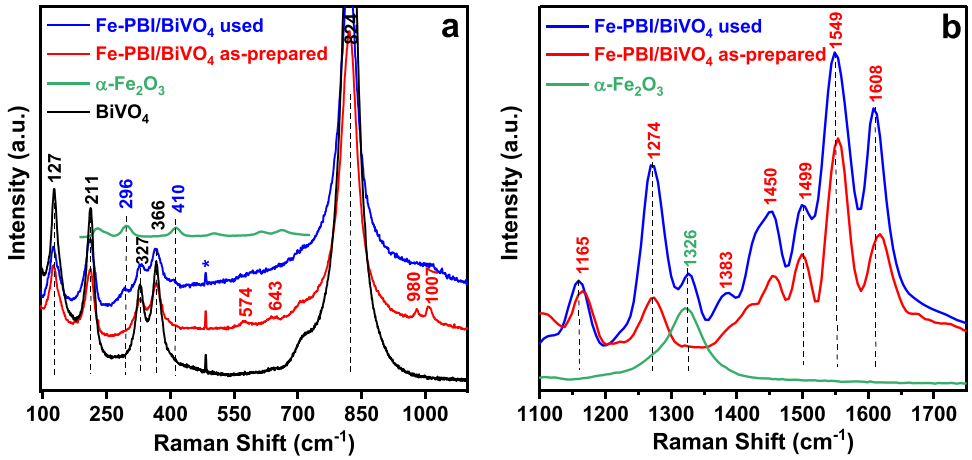

Fig. 10. a) Raman spectra of the as-prepared and used **Fe-PBI/BiVO$_4$**, **BiVO$_4$** and α-Fe_2O_3 photoanodes in the range of 100–1100 cm^{-1}. b) Raman spectra of the same photoanodes in the range of 1100–1750 cm^{-1}. α-Fe_2O_3 phase was identified for the used **Fe-PBI/BiVO$_4$**.

photo-decomposition that can produce the co-catalyst α-Fe_2O_3, but this process does not require external bias or high-energy holes from the semiconductor. Once the PBI ligand is photolyzed from the complex, with or without external bias, the oxo-bridged Fe_2^{III} structural features appear, possibly still containing some PBI ligand residues as evidenced by the Raman peaks in Fig. 12b and illustrated by the hypothesized cluster-like intermediate in Fig. 11. The PBI ligand thus exerts a metallochaperone-like effect regulating the co-catalyst build-up and plays role in photosensitization in the visible range due to the MLCT absorption. Elemental mappings were also recorded on a representative 0.5 × 0.5 mm area of a surface as prepared and another used in PEC, based on the Fe 3p and N 1s peak by XPS (Fig. 12d). The as-prepared surface map corroborated an even distribution of **Fe-PBI**, since the Fe and N atom ratio was 10.8 (expected 9) with Fe 3p and N 1s binding energies corresponding to those in Table 2. In contrast, the Fe to N ratio on the used surface (washed with copious amounts of dichloromethane to remove any trace of organics, or complex residues) was roughly one in accordance with the earlier findings (Table 1), and the binding energies were also in complete agreement with those listed earlier (Fig. 6, Table 2) and assigned to the *in-situ* formed hematite co-catalyst. The distribution of Fe and N were not in line anymore, as seen in Fig. 12d, further implying the formation of hematite. According to the missing N 1s peak at 399.9 eV from the XPS spectrum of the **Fe-PBI/BiVO$_4$** used over 3 h of PEC at 1.5 V_{RHE} the high-energy photogenerated holes in $BiVO_4$ play role in the complete elimination of PBI from the co-catalyst decorated surface.

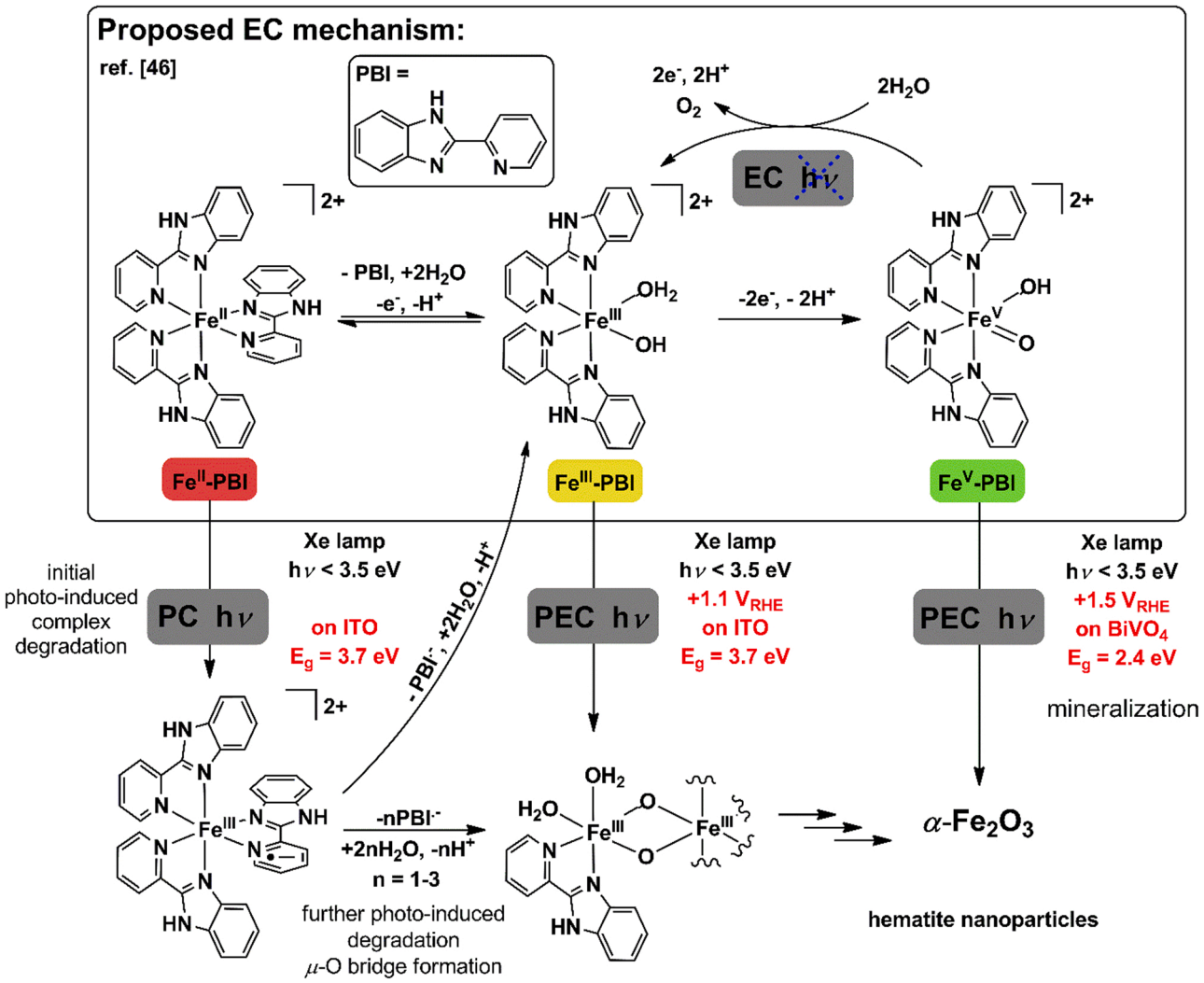

Fig. 11. Proposed mechanisms of electrochemical, photochemical and photoelectrochemical processes occurring on the surface of **Fe-PBI/ITO** and **Fe-PBI/$BiVO_4$** electrodes.

4. Conclusions

In summary, we explored the photoelectrochemical performance of a nanopyramidal **$BiVO_4$** photoanode for water oxidation modified with an iron-derived water-insoluble molecular pre-catalyst. Surface analysis revealed that the true co-catalyst was α-Fe_2O_3 nanoparticles decorated to $BiVO_4$. We found that the pre-catalyst modified **Fe-PBI/$BiVO_4$** photoanode exhibited onset potential lower by 0.6 V and improved charge separation efficiency compared to pristine **$BiVO_4$**. This suggested that the addition of the co-catalyst to **$BiVO_4$** facilitates the transport of holes to the surface by blocking defect sites. In addition, **Fe-PBI/$BiVO_4$** showed higher charge transfer efficiency and lower charge transfer resistance. This we attribute to hole trapping by the iron compound leading to the acceleration of water oxidation by lowering surface recombination at moderate potentials. At higher anodic potentials, the co-catalyst provides additional active, higher-valent iron centers for water oxidation, thus accelerating the reaction. Furthermore, we noticed that the α-Fe_2O_3 nanoparticles deposited on the V vacant area of the $BiVO_4$ blocking those defect sites. While **Fe-PBI/$BiVO_4$** produced oxygen with 84 % Faradaic efficiency in long-term electrolysis, we observed lower performance when $FeCl_3$ or $Fe(NO_3)_3$ precursors were applied on $BiVO_4$. The morphologically favorable, pyramidal-shaped $BiVO_4$ nanowire arrays can be prepared conveniently, at low-cost and larger scales. Our results demonstrate the benefits of using an iron complex as a pre-catalyst that is suitable for morphology-preserving amendment of the synthetically occurring and performance-limiting V-vacant defect sites.

Funding

This work was supported by the National Research, Development and Innovation (NRDI) Fund of Hungary (Hungary); grant numbers NKFI-128841 and TKP2021-NKTA-05, and the National Key Research and Development Program of China (China) (2018YFB1502003). We also thank the Renewable Energy National Laboratory (Hungary) for support, financed by the RRF-2.3.1-21-2022-00009 project. AS gratefully acknowledges the support of the Bolyai Janos Research Fellowship of the HAS and the "UNKP-21-5-SZTE-586" New National Excellence of the Ministry for Innovation and Technology from the source of the NRDI Fund. ZK is grateful for K_21 138714 project for the Hungarian NRDI Office. Project no. TKP2021-NVA-19 has been implemented with the support provided by the Ministry of Innovation and Technology of Hungary from the NRDI Fund, financed under the TKP2021-NVA funding scheme.

CRediT authorship contribution statement

Tímea Benkó: Conceptualization, Methodology, Visualization,

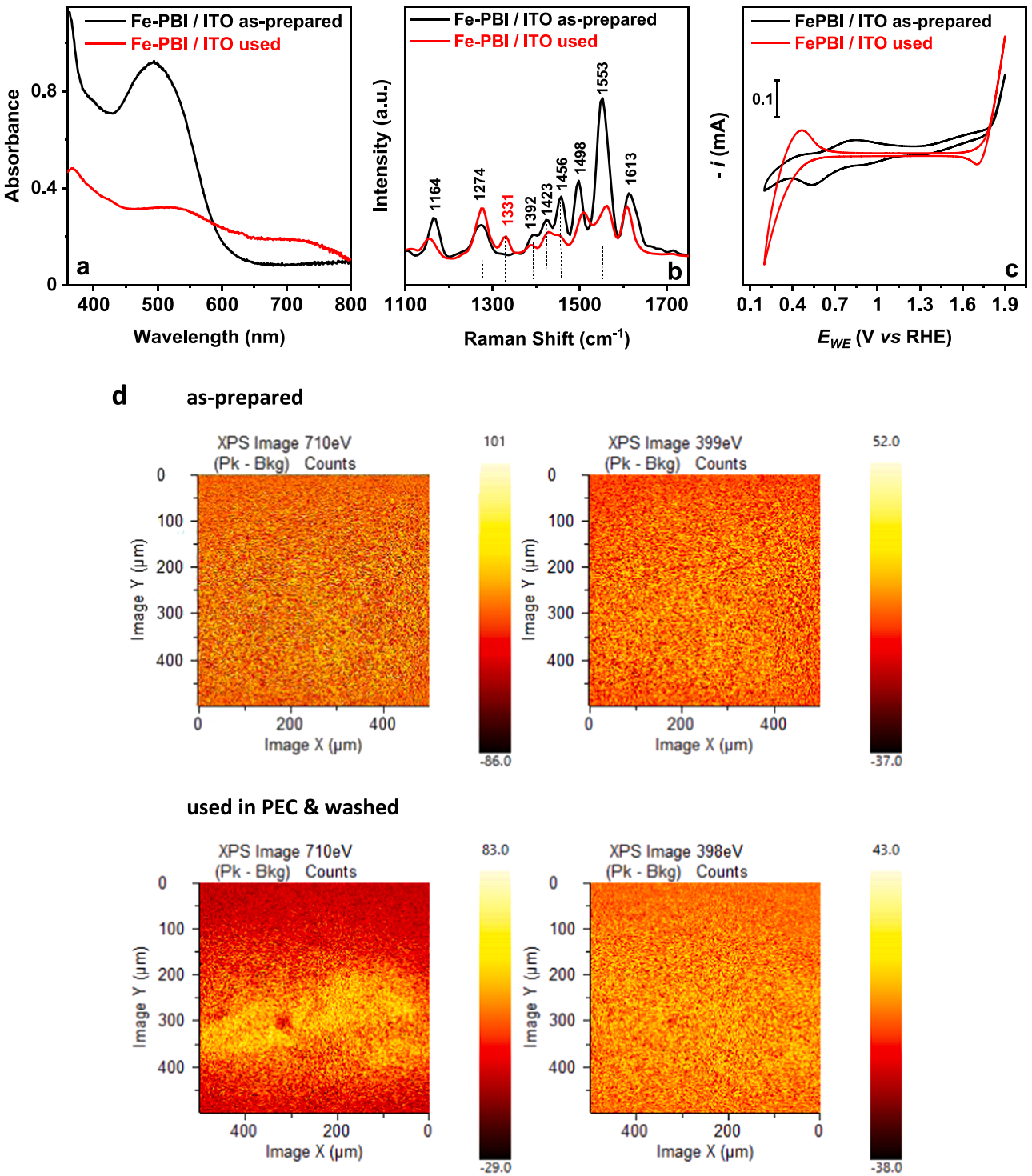

Fig. 12. a) UV–vis absorption spectra of the as-prepared and used **Fe-PBI / ITO** electrodes obtained by DRS. b) Raman spectra of the as-prepared and used **Fe-PBI / ITO** electrodes in the range of 1100–1750 cm^{-1}. c) Cyclic voltammograms of the as-prepared and used **Fe-PBI / ITO** electrodes in 0.2 M borate buffer (pH 8.3, $\nu = 100$ mV/s, Pt aux. and Ag/AgCl ref. electrode). d) Surface compositions of the samples determined by XPS in a Thermo Scientific Escalab Xi+ instrument. The samples were analyzed by using a monochromatized Al K-alpha source (1486.6 eV). On each sample, wide range spectra were collected (at analyzer pass energy of 100 eV) for surveying the elemental composition. For quantitative and chemical state analysis, high-resolution spectra (at 20 eV pass energy) were recorded. The C-C/C-H component of the C 1 s peak was used for calibration (284.8 eV) of the binding energy scale. The pixel color map represents the difference between background and peak photoelectron count numbers within the binding energy region corresponding to Fe 3p (710 eV) or N 1 s (399 eV).

Writing- Original draft preparation **Shaohua Shen:** Resources, Writing- Reviewing and Editing **Miklós Németh:** Visualization, Investigation, Methodology **Jinzhan Su:** Investigation, Methodology **Ákos Szamosvölgyi:** Investigation, Methodology **Zoltán Kovács:** Investigation, Methodology **György Sáfrán:** Investigation, Methodology **Sahir M. Alzuraiji:** Investigation, Methodology **Endre Zsolt Horváth:** Investigation, Methodology **András Sápi:** Writing- Reviewing and Editing **Zoltán Kónya:** Writing- Reviewing and Editing **József Sándor Pap:** Supervision, Conceptualization, Methodology, Visualization, Writing- Reviewing and Editing,

Declaration of Competing Interest

The authors declare that they have no known competing financial interests or personal relationships that could have appeared to influence the work reported in this paper.

Data availability

Data will be made available on request.

Acknowledgements

The authors are grateful to Noémi Szász for the preparation of the TEM samples, to Levente Illés for the SEM measurements and Antal Koós for the Raman measurements.

Appendix A. Supporting information

Supplementary data associated with this article can be found in the online version at doi:10.1016/j.apcata.2023.119035.

References

[1] M.Z. Jacobson, M.A. Delucchi, Z.A.F. Bauer, S.C. Goodman, W.E. Chapman, M. A. Cameron, C. Bozonnat, L. Chobadi, H.A. Clonts, P. Enevoldsen, J.R. Erwin, S. N. Fobi, O.K. Goldstrom, E.M. Hennessy, J. Liu, J. Lo, C.B. Meyer, S.B. Morris, K. R. Moy, P.L. O'Neill, I. Petkov, S. Redfern, R. Schucker, M.A. Sontag, J. Wang, E. Weiner, A.S. Yachanin, Joule 1 (2017) 108–121.
[2] Y. Qi, J. Zhang, Y. Kong, Y. Zhao, S. Chen, D. Li, W. Liu, Y. Chen, T. Xie, J. Cui, C. Li, K. Domen, F. Zhang, Nat. Commun. 13 (2022) 484.
[3] P. Mane, I.V. Bagal, H. Bae, V. Burungale, A.-N. Cha, S.-W. Ryu, S.H. Kang, J.-S. Ha, J. Environ. Chem. Eng. 10 (2022), 106946.
[4] D. Dai, X. Liang, B. Zhang, Y. Wang, Q. Wu, X. Bao, Z. Wang, Z. Zheng, H. Cheng, Y. Dai, B. Huang, P. Wang, Adv. Sci. 9 (2022), 2105299.
[5] L. Wang, Z. Liu, X. Xu, Y. Jia, Q. Mei, F. Ding, J. Peng, Q. Wang, ACS Appl. Energy Mater. 5 (2022) 6383–6392.
[6] Y. Taga, Z. Pan, K. Katayama, W.Y. Sohn, ACS Appl. Energy Mater. 5 (2022) 5750–5755.
[7] C. Xu, W. Sun, Y. Dong, C. Dong, Q. Hu, B. Ma, Y. Ding, J. Mater. Chem. A 8 (2020) 4062–4072.
[8] T. Wang, X. Long, S. Wei, P. Wang, C. Wang, J. Jin, G. Hu, ACS Appl. Mater. Interfaces 12 (2020) 49705–49712.
[9] L. Gao, F. Li, H. Hu, X. Long, N. Xu, Y. Hu, S. Wei, C. Wang, J. Ma, J. Jin, ChemSusChem 11 (2018) 2502–2509.
[10] L. Gao, X. Long, S. Wei, C. Wang, T. Wang, F. Li, Y. Hu, J. Ma, J. Jin, Chem. Eng. J. 378 (2019), 122193.
[11] B. Zhang, L. Chou, Y. Bi, Appl. Catal. B Environ. 262 (2020), 118267.
[12] X. Cao, Y. Wang, J. Lin, Y. Ding, J. Mater. Chem. A 7 (2019) 6294–6303.
[13] M.S. Prévot, K. Sivula, J. Phys. Chem. C 117 (2013) 17879–17893.
[14] J. Su, L. Guo, S. Yoriya, C.A. Grimes, Cryst. Growth Des. 10 (2010) 856–861.
[15] T. Tran-Phu, Z. Fusco, I. Di Bernardo, J. Lipton-Duffin, C.Y. Toe, R. Daiyan, T. Gengenbach, C.-H. Lin, R. Bo, H.T. Nguyen, G.M.J. Barca, T. Wu, H. Chen, R. Amal, A. Tricoli, Chem. Mater. 33 (2021) 3553–3565.
[16] Y. Liu, Y. Guo, L.T. Schelhas, M. Li, J.W. Ager, J. Phys. Chem. C 120 (2016) 23449–23457.
[17] D. Liu, Y. Liu, Z. Zhou, S. Ding, Z. Xia, M. Li, J. Phys. Chem. C 122 (2018) 25195–25203.
[18] J.H. Kim, J.-W. Jang, Y.H. Jo, F.F. Abdi, Y.H. Lee, R. van de Krol, J.S. Lee, Nat. Commun. 7 (2016) 13380.
[19] A. Verma, A. Srivastav, S.A. Khan, V.R. Satsangi, R. Shrivastav, D.K. Avasthi, S. Dass, Phys. Chem. Chem. Phys. 19 (2017) 15039–15049.
[20] S. Bai, H. Chu, X. Xiang, R. Luo, J. He, A. Chen, Chem. Eng. J. 350 (2018) 148–156.
[21] Y. Zhang, L. Shi, Z. Geng, T. Ren, Z. Yang, Sci. Rep. 9 (2019) 19090.
[22] J.A. Seabold, K.-S. Choi, J. Am. Chem. Soc. 134 (2012) 2186–2192.
[23] T.W. Kim, K.-S. Choi, Science 343 (2014) 990–994.
[24] S. Ho-Kimura, W. Luo, Sustain. Energy Fuels 5 (2021) 3102–3114.
[25] D.K. Lee, K.-S. Choi, Nat. Energy 3 (2018) 53–60.
[26] L. Li, J. Li, J. Bai, Q. Zeng, L. Xia, Y. Zhang, S. Chen, Q. Xu, B. Zhou, Nanoscale 10 (2018) 18378–18386.
[27] X. Han, Y. Wei, J. Su, Y. Zhao, ACS Sustain. Chem. Eng. 6 (2018) 14695–14703.
[28] Y. Kuang, Q. Jia, H. Nishiyama, T. Yamada, A. Kudo, K. Domen, Adv. Energy Mater. 6 (2016), 1501645.
[29] M.N. Shaddad, M.A. Ghanem, A.M. Al-Mayouf, S. Gimenez, J. Bisquert, I. Herraiz-Cardona, ChemSusChem 9 (2016) 2779–2783.
[30] L. Xia, J. Bai, J. Li, Q. Zeng, L. Li, B. Zhou, Appl. Catal. B Environ. 204 (2017) 127–133.
[31] B. Zhang, L. Wang, Y. Zhang, Y. Ding, Y. Bi, Angew. Chem. Int. Ed. 57 (2018) 2248–2252.
[32] X. Wan, J. Su, L. Guo, Eur. J. Inorg. Chem. 2018 (2018) 2557–2563.
[33] Y. Lu, J. Su, J. Shi, D. Zhou, ACS Appl. Energy Mater. 3 (2020) 9089–9097.
[34] L. Wang, T. Zhang, J. Su, L. Guo, Nano Res 13 (2020) 231–237.
[35] C. Zachäus, F.F. Abdi, L.M. Peter, R. van de Krol, Chem. Sci. 8 (2017) 3712–3719.
[36] T. Zhang, Y. Lu, J. Wang, Z. Wang, W. Zhang, X. Wang, J. Su, L. Guo, Nanotechnology 31 (2019), 115707.
[37] S. Wang, D. Cui, W. Hao, Y. Du, Energy Fuels (2022).
[38] M.W. Kanan, D.G. Nocera, Science (2008).
[39] S.K. Pilli, T.E. Furtak, L.D. Brown, T.G. Deutsch, J.A. Turner, A.M. Herring, Energy Environ. Sci. 4 (2011) 5028–5034.
[40] S.K. Pilli, T.G. Deutsch, T.E. Furtak, J.A. Turner, L.D. Brown, A.M. Herring, Phys. Chem. Chem. Phys. 14 (2012) 7032–7039.
[41] X. Li, J. Wan, Y. Ma, Y. Wang, X. Li, Chem. Eng. J. 404 (2021), 127054.
[42] M. de Respinis, K.S. Joya, H.J.M. De Groot, F. D'Souza, W.A. Smith, R. van de Krol, B. Dam, J. Phys. Chem. C 119 (2015) 7275–7281.
[43] X. Wan, L. Wang, C.-L. Dong, G. Menendez Rodriguez, Y.-C. Huang, A. Macchioni, S. Shen, ACS Energy Lett. 3 (2018) 1613–1619.
[44] B. Liu, J. Li, H.-L. Wu, W.-Q. Liu, X. Jiang, Z.-J. Li, B. Chen, C.-H. Tung, L.-Z. Wu, ACS Appl. Mater. Interfaces 8 (2016) 18577–18583.
[45] Y. Wang, F. Li, X. Zhou, F. Yu, J. Du, L. Bai, L. Sun, Angew. Chem. 129 (2017) 7015–7019.
[46] Y. Wang, F. Li, H. Li, L. Bai, L. Sun, Chem. Commun. 52 (2016) 3050–3053.
[47] W. Jiang, X. Yang, F. Li, Q. Zhang, S. Li, H. Tong, Y. Jiang, L. Xia, Chem. Commun. 55 (2019) 1414–1417.
[48] Y. Liu, Y. Jiang, F. Li, F. Yu, W. Jiang, L. Xia, J. Mater. Chem. A 6 (2018) 10761–10768.
[49] T. Tian, C. Dong, X. Liang, M. Yue, Y. Ding, J. Catal 377 (2019) 684–691.
[50] S. Zhou, P. Yue, J. Huang, L. Wang, H. She, Q. Wang, Chem. Eng. J. 371 (2019) 885–892.
[51] X. Cao, C. Xu, X. Liang, J. Ma, M. Yue, Y. Ding, Appl. Catal. B Environ. 260 (2020), 118136.
[52] B. Gao, T. Wang, X. Fan, H. Gong, P. Li, Y. Feng, X. Huang, J. He, J. Ye, J. Mater. Chem. A 7 (2018) 278–288.
[53] Y. Shang, F. Niu, S. Shen, Chin. J. Catal. 39 (2018) 502–509.
[54] Y. Shi, Y. Yu, Y. Yu, Y. Huang, B. Zhao, B. Zhang, ACS Energy Lett. 3 (2018) 1648–1654.
[55] S.M. Al-Zuraiji, T. Benkó, L. Illés, M. Németh, K. Frey, A. Sulyok, J.S. Pap, J. Catal. 381 (2020) 615–625.
[56] J.S. Pap, A. Draksharapu, M. Giorgi, W.R. Browne, J. Kaizer, G. Speier, Chem. Commun. 50 (2014) 1326–1329.
[57] K. Nie, S. Kashtanov, Y. Wei, Y.-S. Liu, H. Zhang, M. Kapilashrami, Y. Ye, P.-A. Glans, J. Zhong, L. Vayssieres, X. Sun, J. Guo, Nano Energy 53 (2018) 483–491.
[58] P. Makuła, M. Pacia, W. Macyk, J. Phys. Chem. Lett. 9 (2018) 6814–6817.
[59] J.K. Cooper, S. Gul, F.M. Toma, L. Chen, Y.-S. Liu, J. Guo, J.W. Ager, J. Yano, I. D. Sharp, J. Phys. Chem. C 119 (2015) 2969–2974.
[60] R. Yalavarthi, R. Zbořil, P. Schmuki, A. Naldoni, Š. Kment, J. Power Sources 483 (2021), 229080.
[61] F.F. Abdi, R. van de Krol, J. Phys. Chem. C 116 (2012) 9398–9404.
[62] Y. Qiu, W. Liu, W. Chen, W. Chen, G. Zhou, P.-C. Hsu, R. Zhang, Z. Liang, S. Fan, Y. Zhang, Y. Cui, Sci. Adv. 2 (n.d.) e1501764.
[63] L.M. Peter, K.G.U. Wijayantha, A.A. Tahir, Faraday Discuss. 155 (2012) 309–322.
[64] S.Y. Jeong, K.S. Choi, H.-M. Shin, T.L. Kim, J. Song, S. Yoon, H.W. Jang, M.-H. Yoon, C. Jeon, J. Lee, S. Lee, ACS Appl. Mater. Interfaces 9 (2017) 505–512.
[65] J. Li, L. Guo, N. Lei, Q. Song, Z. Liang, ChemElectroChem 4 (2017) 2852–2861.
[66] C. Ding, J. Shi, Z. Wang, C. Li, ACS Catal. 7 (2017) 675–688.
[67] W. Zhang, J. Ma, L. Xiong, H.-Y. Jiang, J. Tang, ACS Appl. Energy Mater. 3 (2020) 5927–5936.
[68] Y. Zhang, H. Zhang, H. Ji, W. Ma, C. Chen, J. Zhao, J. Am. Chem. Soc. 138 (2016) 2705–2711.
[69] X. Lu, K. Ye, S. Zhang, J. Zhang, J. Yang, Y. Huang, H. Ji, Chem. Eng. J. 428 (2022), 131027.
[70] S. Kalantarifard, R. Bikas, S. Nandy, T. Lis, K.H. Chae, M.M. Najafpour, J. Phys. Chem. C (2022).
[71] A.P. Grosvenor, B.A. Kobe, M.C. Biesinger, N.S. McIntyre, Surf. Interface Anal. 36 (2004) 1564–1574.
[72] S. Wang, X. Wang, B. Liu, Z. Guo, K. Ostrikov, L. Wang, W. Huang, Nanoscale (2021).
[73] K.R. Tolod, S. Hernández, M. Castellino, F.A. Deorsola, E. Davarpanah, N. Russo, Int. J. Hydrogen Energy 45 (2020) 605–618.
[74] S. Zhang, M. Rohloff, O. Kasian, A.M. Mingers, K.J.J. Mayrhofer, A. Fischer, C. Scheu, S. Cherevko, J. Phys. Chem. C 123 (2019) 23410–23418.
[75] J.F. Moulder, J. Chastain. Handbook of X-Ray Photoelectron Spectroscopy: A Reference Book of Standard Spectra for Identification and Interpretation of XPS Data, Physical Electronics Division, Perkin-Elmer Corp., Eden Prairie, Minn., 1992.
[76] G.C. Allen, M.T. Curtis, A.J. Hooper, P.M. Tucker, J. Chem. Soc. Dalton Trans. (1974) 1525–1530.
[77] A.N. Mansour, R.A. Brizzolara, Surf. Sci. Spectra 4 (1996) 351–356.
[78] Y.-X. Zhang, Y. Jia, Appl. Surf. Sci. 290 (2014) 102–106.
[79] Y. Jia, T. Luo, X.-Y. Yu, Z. Jin, B. Sun, J.-H. Liu, X.-J. Huang, N. J. Chem. 37 (2013) 2551–2556.
[80] Y. Wei, J. Su, X. Wan, L. Guo, L. Vayssieres, Nano Res 9 (2016) 1561–1569.
[81] L. Wang, J. Su, L. Guo, Nano Res 12 (2019) 575–580.
[82] M. Zheng, X. Cao, Y. Ding, T. Tian, J. Lin, J. Catal. 363 (2018) 109–116.
[83] M.R. da, S. Pelissari, N.F. Azevedo Neto, L.P. Camargo, L.H. Dall'Antonia, Electrocatalysis 12 (2021) 211–224.
[84] G.M. Kuramshina, O.A. Vakula, N.I. Vakula, A.G. Majouga, V.M. Senyavin, L. G. Gorb, J. Leszczynski, Struct. Chem. 27 (2016) 209–219.

[85] P. Kumar, H. No-Lee, R. Kumar, J. Mater. Sci. Mater. Electron. 25 (2014) 4553–4561.
[86] D.L.A. de Faria, S. Venâncio Silva, M.T. de Oliveira, J. Raman Spectrosc. 28 (1997) 873–878.
[87] R. Hoshikawa, K. Yoshida, R. Mitsuhashi, M. Mikuriya, T. Okuno, H. Sakiyama, Molecules 26 (2021) 897.
[88] J.L. Lee, S. Biswas, C. Sun, J.W. Ziller, M.P. Hendrich, A.S. Borovik, J. Am. Chem. Soc. 144 (2022) 4559–4571.
[89] H. Zheng, Y. Zang, Y. Dong, V.G. Young, L. Que, J. Am. Chem. Soc. 121 (1999) 2226–2235.
[90] R.E. Norman, R.C. Holz, S. Menage, L. Jr, Que, J.H. Zhang, C.J. O'Connor, Inorg. Chem. 29 (1990) 4629–4637.
[91] X. Zong, S. Thaweesak, H. Xu, Z. Xing, J. Zou, G. (Max) Lu, L. Wang, Phys. Chem. Chem. Phys. 15 (2013) 12314–12321.
[92] N.A. Arzaee, M.F. Mohamad Noh, A.A. Halim, M.A. Faizal Abdul Rahim, N. S. Haziqah Mohd Ita, N.A. Mohamed, S.N. Farhana Mohd Nasir, A.F. Ismail, M. A. Mat Teridi, J. Alloy. Compd. 852 (2021), 156757.
[93] G. Mathew, P. Dey, R. Das, S.D. Chowdhury, M. Paul Das, P. Veluswamy, B. Neppolian, J. Das, Biosens. Bioelectron. 115 (2018) 53–60.
[94] J. Wang, J.L. Waters, P. Kung, S.M. Kim, J.T. Kelly, L.E. McNamara, N.I. Hammer, B.C. Pemberton, R.H. Schmehl, A. Gupta, S. Pan, ACS Appl. Mater. Interfaces 9 (2017) 381–390.